Prodding Magnetic Properties of Electrodeposited Co/Cu and Ni/Cu alloy Films by Scanning Probes

A thesis submitted in partial fulfillment of the requirement for the award of degree of

Masters of Technology
In
Metallurgical and Materials Engineering

Submitted by
Arpita Das
Roll No. 208MM104

Department of Metallurgical and Materials Engineering
National Institute of Technology,
Rourkela-769008,
2010

Prodding Magnetic Properties of Electrodeposited Co/Cu and Ni/Cu alloy Films by Scanning Probes

A thesis submitted in partial fulfillment of the requirement for the award of degree of

Masters of Technology
In
Metallurgical and Materials Engineering

Submitted by
Arpita Das
Roll No. 208MM104

Under the Supervision Of

Prof. Archana Mallik

Prof B.C.Ray

Department of Metallurgical and Materials Engineering
National Institute of Technology,
Rourkela-769008,

2010

National Institute of Technology
Rourkela

Certificate

This is to certify that the thesis entitled **"Prodding the Magnetic Properties of Electrodeposited Co/Cu and Ni/Cu films by Scanning Probes"** submitted by Arpita Das in partial fulfillment of the requirements for the award of Masters of Technology in Metallurgical and Materials Engineering with specialization in "Metallurgical and Materials Engineering" at National Institute of Technology, Rourkela (Deemed University) is an authentic work carried out by her under our supervision and guidance.

To the best of our knowledge, the matter embodied in the thesis has not been submitted to any other university/Institute for the award of any Degree or Diploma.

Date -

Supervisor

Prof. Archana Mallik
Metallurgical and Materials Engg.
National Institute of Technology,
Rourkela-769008

Co-Supervisor

Prof. B. C. Ray
Metallurgical and Materials Engg.
National Institute of Technology,
Rourkela-769008

TABLE OF CONTENTS

Chapter-4

Acknowledgement

I take this opportunity to express my deep regards and sincere gratitude for this valuable, expert guidance rendered to me by guide Prof. Archana Mallik, Assistant Professor, Department of Metallurgical and Materials Engineering, National Institute of Technology, Rourkela and Prof B.C Ray, Professor, Department of Metallurgical and Materials Engineering, National Institute of Technology, Rourkela. I consider me fortunate to have had opportunity to work under their guidance and enrich myself from their vast knowledge and analysis power. They will always be constant source of inspiration for me.

My sincere thanks to Dr. B. B. Verma, Professor and Head Metallurgical and Materials Engineering Department for his talented advice and providing necessary facility for my work.

I would also take this opportunity to express my gratitude and sincere thanks to my honorable teachers for their invaluable advice, constant help, encouragement, inspiration and blessing.

I am also thankful to laboratory members of Department of Metallurgical and Materials Engineering, NIT Rourkela, especially, R. Pattanaik, U. K. Sahu for constant practical assistance and help whenever required.

Special thanks to my parents, friends and other members of the department for being so supportive and helpful in every possible way.

Arpita Das

List of figures

List of Tables

List of original publications

1. A. Mallik, **A. Das,** S. Rout: Effect of plating parameters on the magnetic structure distribution in electrodeposited Co/Cu magnetic alloy thin films: An analysis by MFM, ***Journal of Magnetism and Magnetic Materials:*** MAGMAD-10-00544 [submitted].

2. A. Mallik, **A. Das:** MFM analysis on the magnetic structure distribution in electrodeposited Cu/Ni magnetic alloy thin films: Effect of plating parameters [In submission].

3. **A. Das,** A.Mallik, B.C.Ray: Chronoamperomatric and Structural studies of Potentiostatistically electrodeposited Nickel in presence of Ultrasound, **Recent Trends in Materials and Characterization (RETMAC-2010)"**, 14-15 February 2010, National Institute of Technology, Suratkal, Karnataka, India.

4. **A.Das,** A.Mallik, B.C.Ray: Prodding the magnetic properties of Electrodeposited Nickel by Magnetic Force Microscope (MFM), **3rd National Symposium for Materials Research Scholars MR-10,** 7-8/05/2010, IIT Bombay, India. ***Awarded Best Oral Perentation in Magnetic & Electric Material***.

Beyond the scope of the current research

1. A. Mallik, S. Rout, **A. Das:** Approaches to understand the non-isothermal grain growth behavior of sono-electrochemically deposited Cu thin film, ***Journal of Applied Physics:*** JR 10-2994 [submitted], , Beyond the scope of the project topic.

Abstract

Magnetic thinfilms, either granular or multilayed, are essential components for the design of magnetic devices. In order to design magnetic material for specific application, it is necessary to understand the influence of preparation process and preparation materials on the resulting parameter such as grain size and magnetic structure. Magnetic domain structure is responsible for the magnetic behavior of ferromagnetic material. Magnetic domains are the regions having uniform magnetization. There are different energies acting in a magnetic system. Domain structure always has its origin in the possibility of lowering the energy of the system by going from a saturated configuration with magnetic energy to a domain configuration with a lower energy. Magnetic force microscope technique provides the internal structure of domain walls and the spin distributions within domains as well as the general feature of the domain structure. During MFM measurement, there are two forces acting on the tip: magnetic and Vander wall's forces. Hence in MFM, the signal contains both information of surface topography and surface magnetic property generated by Vander Waal's and magnetic forces respectively. MFM can image domain structure in various recording media, materials, and superconductor or, increasingly, small particles, all with sub 100 nm special resolutions. In this work we prepare the Cu, Co and Ni thin films with Co-Cu alloy and Ni-Cu alloy thin film by electrodeposition method at different deposition potential and concentration of electrolyte at 25°C Films are characterized by XRD, SEM, and MFM. Scahifker and Hills model was used for study of nucleation and growth phenomena for electrochemically deposited thin film by cyclic voltammetry and chronoamperometry.

Different deposition potentials were selected for the deposition for all the films. To set the deposition potential in all the systems Cyclic Voltammetry is done. The thickness of films lies in the range of 300-400 nm. The phases of the deposits are confirmed by the XRD analysis. As the deposition potential increases the crystallite size of the deposits decreases which is also confirmed by the morphological analysis by SEM. Magnetic domain structure and topography is analyzed by MFM. The topographic figure indicates the presence of aggregates of different sizes on the electrode surface. The films contain two distinct areas, one plane and the other with random fluctuations. The plane regions are assumed to have no contribution to the phase shift of

the tip, remarked as non-magnetic phase. As Cu concentration decreases in the alloy solution, the domains are larger in size.

CHAPTER -1

Introduction

Evolution of magnetic thin film
Motivation
Objectives
Thesis Outlines

1.1. Evolution of magnetic thin films

Since the early nineties, there has been tremendous interest in magnetic materials with nanoscale dimensions for various applications. The reduction in dimension of thin magnetic films is responsible for new physical properties due to the great influence of surfaces and interfaces. As the size of the electronic devices shrink, the charge and the spin degrees of freedom must be considered to understand their transport properties. In thin films the magnetic properties can get influenced significantly by internal stresses generated during deposition as well as by surface irregularities [1]. The increasing of data storage density imposes the need of a material consisting of magnetically isolated grains with a sized of few nanometers [2]. Development of a soft magnetic recording head material with high saturation magnetic flux density and low coercivity is a prerequisite for realizing magnetic storage devices with a high areal recording density [3]. The properties of magnetic thin film depend on the film thickness. Conventional techniques are inadequate to manufacture micromagnets, whereas electrodeposition of permanent micromagnets is a simple and low cost manufacturing technique, which would allow the production of magnetic devices with controlled geometry, like proximity sensors, electric wrist watches, microactuators or micromotors. Electrodeposition is also a suitable alternative rechnique for the easy control of structure growth and shape of the electrodeposited magnetic films at microscopic level. Alloys are typically deposited from a single electrolyte which contains the required metal cations in solution in concentration quite different from those required in the metal film. Much interest has been growing toward the electrodeposition of Cobalt alloy films due to extensive application in perpendicular high density magnetic recording media and micromagnets. Electrodeposited elemental Nickel has been the material of choice to demonstrate a variety of microdevice prototypes, including micro-gears and micro-cantilevers. Ni-Cu alloys have great potentials in industrial applications where resistance to corrosion and thermoelectric characteristics are requirements. Its corrosion resistance makes it possible for use as a protective coating in marine and corrosive environment [4]. The bath composition has an enormous effect on the electrodeposited thin film. The magnetic force microscopy (MFM) is one of the most useful experimental techniques that have been developed for the study and characterization of physical quantities in a number of materials [5]. The alignment of magnetic domains ultimately reflects on magnetic properties of the films.

1.2. Motivation

Magnetic properties of the magnetic thin films and magnetic alloy thin films are dependent on the concentration of the electrodeposition bath, deposition bath, temperature, current density and P^H of the electrolyte. The aim of the project is to quantify the magnetic microstructure of the magnetic alloy thin film at different bath concentration and different deposition potential at a room temperature. And to verify the dependence of the deposition potential and concentration of the alloy bath on the magnetic microstructure of the deposits.

1.3. Objectives

The overall objectives to be achieved in this study are:

- Co-Cu and Ni-Cu alloy synthesis by electrolytic deposition method.
- Phase and Morphology analysis by XRD and SEM.
- Enumeration of magnetic behavior of alloy by MFM.
- Exploration on the use of films in microelectronics.

1.4. Thesis Outline

The present work has been carried out with an aim to understand nucleation, growth mechanism and the effect of different operating parameters on the morphology and magnetic properties of electrochemically deposited elemental metals (Cu, Ni, Co) and alloy (Ni-Cu and Co-Cu) thin film. The alloy thin films have been prepared at varying Cu concentrations and deposition potentials.

Chapter 2 covers the literature underlying the basic principles of magnetism, magnetic materials, magnetic thin film, factors affecting the magnetic properties, different techniques to characterize magnetic property, Magnetic Force microscopy techniques. Different approaches for magnetic thin film preparation have been covered briefly with a wide spectrum for electrodeposition. And the chapter concludes with the basic aims of the project work

Chapter 3 deals with methods & materials and the various characterization techniques used to synthesize and characterize the elemental (Cu, Ni, Co) and alloy (Co-Cu and Ni0Cu) thin films. The synthesis and electrochemical analysis portions include the description of cyclic voltammetry and chronoamperometry techniques in detail. The phase analysis study was described by the understanding of X-ray diffraction (XRD) technique. Morphological structural characterization is understood by the scanning electron microscope (SEM) and Magnetic structure studied by Magnetic force microscopy (MFM) methods.

Results and discussion are covered in chapter 4. Cyclic voltammetry for different systems have been carried out to set the deposition potential and to study the electrochemical aspects. The details are used for the final synthesis of films at a condition with varying parameters. The chronoamperometric current transients are explained and analyzed. XRD has been properly used for the phase identification. The surface morphologies are characterized by SEM. And magnetic characterization was done by MFM. The analysis confirms the finer deposit with increasing deposition potential, increasing Cu concentration. The result shows values corresponding to the obtained results from the characterization part.

Conclusions enlist the detailed in the chapter 5 results obtained from chapter 4. Finally a list of references has been included referred for the preparation of the thesis. However, the work needs further amplification to explore the domain structure with the scanning probes (MFM) at various parameters.

CHAPTER -2

Background

Magnetism and magnetic material
Magnetic domain
Energy consideration of domain structure
Magnetic thin film
Principle of Magnetic Force Microscope (MFM)
Electrochemical Synthesis

2.1.Magnetism and Magnetic materials:

The term Magnetism is used to describe how materials respond on the microscopic level to an applied magnetic field; to categorize the magnetic phase of a material. For example, the most well known form of magnetism is ferromagnetism such that some ferromagnetic materials produce their own persistent magnetic field. However, all materials are influenced to greater or lesser degree by the presence of a magnetic field. Some are attracted to a magnetic field (paramagnetism), others are repulsed by a magnetic field (diamagnetism), and some have a much more complex relationship with an applied magnetic field. Substances that are negligibly affected by magnetic fields are known as non-magnetic substances. They include copper, aluminium, water, gases, and plastic [6-9].

The magnetic state (or phase) of a material depends on temperature (and other variables such as pressure and applied magnetic field) so that a material may exhibit more than one form of magnetism depending on its temperature etc [10].

Never before has our daily life and environment been so significantly dependent on materials with outstanding magnetic properties. Modern life is today in many aspects an automated world which uses ferro- and ferromagnetic materials in nearly all important technical fields as, e.g., electrical power, mechanical power, high-power electromotors, miniature motors, computer technique, magnetic high-density recording, telecommunication, navigation, aviation and space operations, automation micromechanics, medicine, sensor techniques, magnetocaloric refrigeration, materials testing and household applications.

Here only a brief review of advanced magnetic materials used today will be given. These materials in general have a nanocrystalline (NC) structure or, in the case of thin films, at least one dimension is in the nanometer scale.

- High-permeability nc-materials based on Fe_3Si with additives of Cu, Nb, Zr, B (Finemet) achieve permeabilities up to $10^5 – 10^6$ [11].
- High-coercivity nc-magnets based on $Nd_2Fe_{14}B$ and CoSm alloys with coercive fields of 1.5 T for NdFeB and up to 3.5 T for Sm_2Co_{17}-based magnets. Maximum energy products of technical magnets of 450 kJ/m^3 energy have been achieved. The development of composite materials has started [12-14].

- Giant-magnetostrictive nc-magnets with $\lambda \geq 10^{-3}$ based on (FeTbDy)-alloys for micromechanic applications [15].
- Giant-magnetoresistive (GMR) thin film systems for read heads with magnetoresistances $\Delta R/R > 50\%$ and high permeability. Examples of multilayer systems are CoFe/Cu or Fe/Co. Systems of GMR films are used to develop nonvolatile "Magnetic Random Access Memories" (MRAM) [16].
- Colossal-magnetoresistive films of LaSr- and LaCa- Manganites with $\Delta R/R > 100\%$ [17, 18].
- Giant-magnetocaloric refrigerator material as $Gd_5(Si_2Ge_2)$ with $\Delta T > 20$ K effects [19].
- Molecular magnets based on metal-organic compounds based on hexafluoroacetylacetonat or tetracyanomethylen.
- Self-organized superlattices of ferromagnetic nanoparticles of FePt or FeCo for high-density recording (Tbit/inch2).
- Computational solid state physics for the calculation of intrinsic material properties and phase diagrams.
- Computational micromagnetism of magnetic ground states and the dynamics of magnetization processes in nc materials, thin platelets and small particles.

2.2. Diamagnetism:

Diamagnetism appears in all materials, and is the tendency of a material to oppose an applied magnetic field, and therefore, to be repelled by a magnetic field. However, in a material with paramagnetic properties (that is, with a tendency to enhance an external magnetic field), the paramagnetic behavior dominates. Thus, despite its universal occurrence, diamagnetic behavior is observed only in a purely diamagnetic material. In a diamagnetic material, there are no unpaired electrons, so the intrinsic electron magnetic moments cannot produce any bulk effect. In these cases, the magnetization arises from the electrons' orbital motions, which can be understood classically as follows:

When a material is put in a magnetic field, the electrons circling the nucleus will experience, in addition to their Coulomb attraction to the nucleus, a Lorentz force from the magnetic field. Depending on which direction the electron is orbiting, this force may increase the centripetal

force on the electrons, pulling them in towards the nucleus, or it may decrease the force, pulling them away from the nucleus. This effect systematically increases the orbital magnetic moments that were aligned opposite the field, and decreases the ones aligned parallel to the field (in accordance with Lenz's law). This results in a small bulk magnetic moment, with an opposite direction to the applied field. All materials undergo this orbital response. However, in paramagnetic and ferromagnetic substances, the diamagnetic effect is overwhelmed by the much stronger effects caused by the unpaired electrons [20-22].

2.3.Paramagnetism:

In a paramagnetic material there are unpaired electrons, i.e. atomic or molecular orbitals with exactly one electron in them. While paired electrons are required by the Pauli Exclusion Principle to have their intrinsic ('spin') magnetic moments pointing in opposite directions, causing their magnetic fields to cancel out, an unpaired electron is free to align its magnetic moment in any direction. When an external magnetic field is applied, these magnetic moments will tend to align themselves in the same direction as the applied field, thus reinforcing it [23, 24].

2.4. Ferromagnetism:

A ferromagnet, like a paramagnetic substance, has unpaired electrons. However, in addition to the electrons' intrinsic magnetic moments tendency to be parallel to an applied field, there is also in these materials a tendency for these magnetic moments to orient parallel to each other to maintain a lowered energy state. Thus, even when the applied field is removed, the electrons in the material maintain a parallel orientation [25, 26].

Every ferromagnetic substance has its own individual temperature, called the Curie temperature, or Curie point, above which it loses its ferromagnetic properties. This is because the thermal tendency to disorder overwhelms the energy-lowering due to ferromagnetic order.

Some well-known ferromagnetic materials that exhibit easily detectable magnetic properties (to form magnets) are nickel, iron, cobalt, gadolinium and their alloys [27].

2.4.1. Magnetic Domain:

The magnetic moment of atoms in a ferromagnetic material cause them to behave something like tiny permanent magnets. They stick together and align themselves into small regions of more or less uniform alignment called magnetic domains or Weiss domains. Magnetic domains can be observed with a magnetic force microscope to reveal magnetic domain boundaries that resemble white lines in the sketch. There are many scientific experiments that can physically show magnetic fields [28-30].

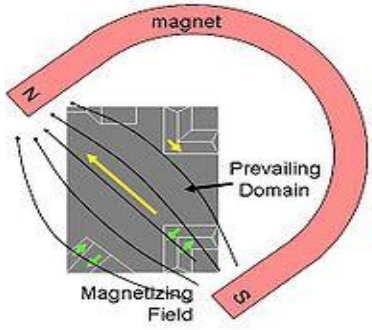

Fig (2.1): Effect of a magnet on the domains.

When a domain contains too many molecules, it becomes unstable and divides into two domains aligned in opposite directions so that they stick together more stably as shown at the right.

When exposed to a magnetic field, the domain boundaries move so that the domains aligned with the magnetic field grow and dominate the structure as shown at the left. When the magnetizing field is removed, the domains may not return to an unmagnetized state. This result in the ferromagnetic material's being magnetized, forming a permanent magnet.

When magnetized strongly enough that the prevailing domain overruns all others to result in only one single domain, the material is magnetically saturated. When a magnetized ferromagnetic material is heated to the Curie point temperature, the molecules are agitated to the point that the magnetic domains lose the organization and the magnetic properties they cause cease. When the material is cooled, this domain alignment structure spontaneously returns, in a manner roughly analogous to how a liquid can freeze into a crystalline solid [31].

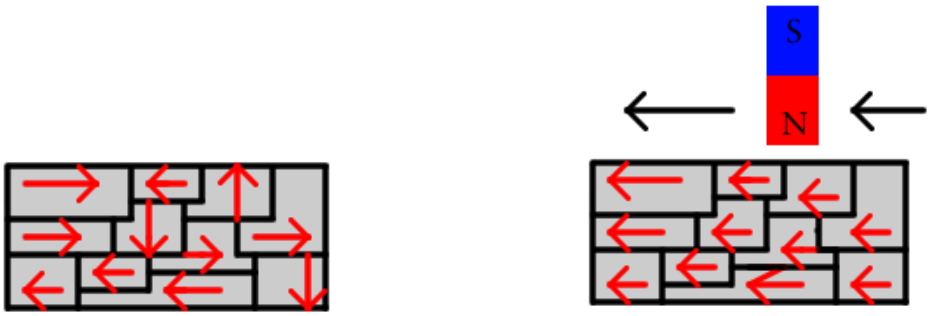

(Unmagnetized) (Magnetized)

Fig (2.2): Domain structure in the unmagnetized and magnetized state

Magnetic domain structure is responsible for the magnetic behavior of ferromagnetic material like Iron, Cobalt and Nickel. The regions separating magnetic domains are called domain wall where the magnetization rotates coherently from the direction in one domain to that in the next domain [32].

2.4.2. Energy consideration for the Magnetic domain:

The existence of magnetic domains is a result of energy minimization. Landau and Lifshitz proposed the theoretical domain structure based on a minimum energy concept, which forms the basis for modern domain theory. The primary reason for the existence of domains within the crystals is that their formation reduces the magnetic free energy. In the simplest case for such a crystal, the energy, "E" is the sum of several free energy terms [33-35].

$$E = E_{ex} + E_k + E_\lambda + E_D + E_H \qquad (1.1)$$

Where, E_{ex} is the Exchange energy.

E_k is the Magnetocrystalline anisotropy energy.

E_λ is the Magnetoelastic energy.

E_D is the Magnetostatic energy.

E_H is the Zeeman energy.

Magnetocrystalline anisotropy energy: The crystal lattice is easy to magnetize in some direction and hard to magnetize in others. Magnetization in the easy direction lowers this energy.

Magnetoeleastic energy: This energy is due to the effect of magnetorestriction, a slight change in the dimensions of the crystal when magnetized. This causes elastic strains in the lattice, and the direction of magnetization that minimizes these strain energies will be favored.

Magnetostatic energy: This is a self energy, due to the interaction of the magnetic field created by the magnetization in some part of the sample on the other part of the same sample. Intrinsically, it has exactly the same nature as the "Zeeman energy" but the interaction of the material with itself is put in the magnetostatic energy whereas the interaction with the external magnetic field is put in the Zeeman energy. This energy term is the only one responsible for the presence of magnetic domains in magnetic materials. Minimization its value requires that the magnetization in the material makes closed loops, with the magnetizations staying parallel to the sample edges.

Zeeman Energy: Energy resulting from the interaction between the magnetic material and an externally applied magnetic field.

So far we have been discussing hypothetical magnetic particles that are uniformly magnetized. Particles with strong magnetizations (like magnetite) have self energies that quickly become quite large because of the dependence on the square of the magnetization. We have been learning about several mechanisms that tend to align magnetic spins. In fact in very small particles of magnetite (< 40 nm), the spins are essentially lined up. The particle is uniformly magnetized and we called it single domain (SD). In larger particles (~80 nm) the self energy exceeds the other exchange and magnetocrystalline energies and crystals have distinctly non-uniform states of magnetization.

There are many strategies possible for magnetic particles to reduce self energy. Numerical models (called micromagnetic models) can find internal magnetization configurations that minimize the energies discussed in the above. Micromagnetic simulations for magnetite particles (e.g. Schabes and Bertram, 1988) allow us to peer into the state of magnetization inside magnetic particles. These particles share many properties of the uniformly magnetized single domain particles and are called pseudo-single domain (PSD) particles.

As particles grow larger (>~200 nm), they break into multiple magnetic domains, separated by narrow zones of rapidly changing spin directions called domain walls. Magnetic domains can take many forms. We illustrate a few in Figure 2.3. The uniform case (single domain) is shown in Figure 2.3(a). The external field is very large because the free poles are far apart (at opposite ends of the particle). When the particle organizes itself into two domains in Figure 2.3(b), the external field is reduced by about a factor of two. In the case of four lamellar domains in Figure 2.3(c), the external field is quite small. The introduction of closure domains as in Figure 2.3(d) reduces the external field to nothing.

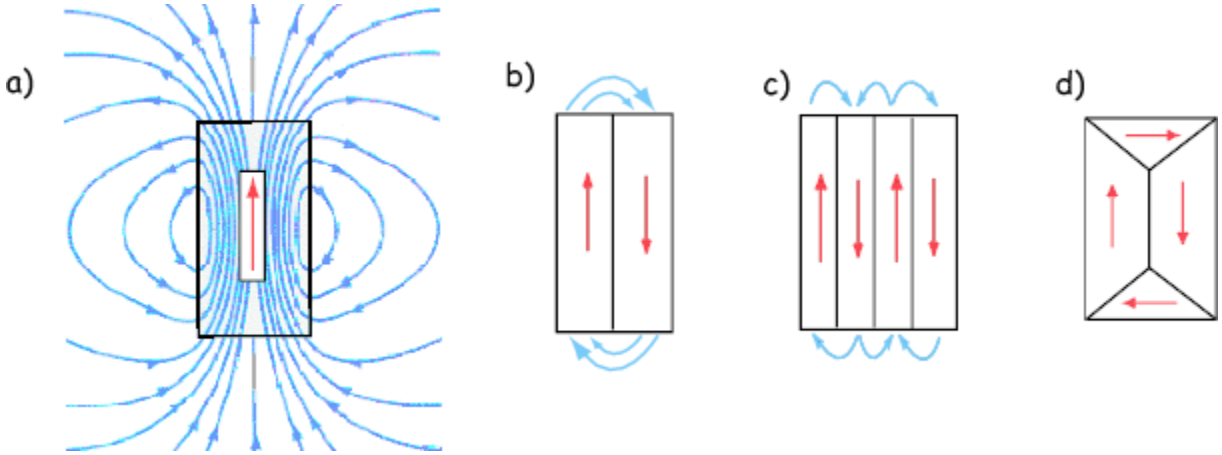

Fig (2.3): A variety of domain structures of a given particle. a) Uniformly magnetized (single domain). b) Two domains. c) Four domains in a lamellar pattern. d) Essentially two domains with two closure domains

Magnetic domain walls are the regions with large stray fields (as opposed to domains in which the spins are usually parallel to the sides of the crystals to minimize stray fields). Domain walls are not "free". If, as in Figure 2.4(a), the spins simply switch from one orientation to the other abruptly, the exchange energy cost would be very high. One way to get around this to spread the change over several hundred atoms, as sketched in Figure 2.4(b). The wall width δ is wider and the exchange energy price is much less. However, there are now spins in unfavorable directions from a magnetocrystalline point of view (they are in "hard" directions). Exchange energy therefore favors wider domain walls while magnetocrystalline anisotropy favors thin walls. With some work, it is possible to come up with the following analytical expressions for wall width (δ_w) and wall energy density (ϵ_w):

$$\delta_w = \pi(\frac{A}{K})^{\frac{1}{2}}, \epsilon_w = 2\pi(AK)^{\frac{1}{2}}, \tag{2.2}$$

where, A is the exchange constant.

K is the magnetic anisotropy constant.

ϵ_w is the energy density per unit wall area, not per volume.

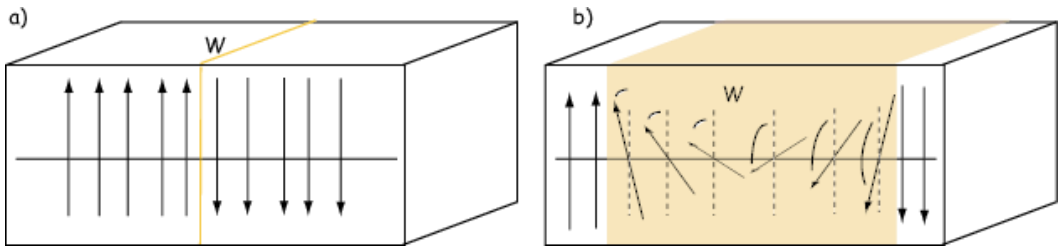

Fig (2.4): Examples of possible domain walls. a) There is a 180° switch from one atom to the next. The domain wall is very thin, but the exchange price is very high. b) There is a more gradual switch from one direction to the other [each arrow represents several 10's of unit cells].

2.5.Different Techniques for the Magnetic characterization:

The domain structure can be characterized qualitatively as well as quantitatively by different techniques. These are;

(i) Magnetization Curve (Hysteresis Loop).

(ii) Magnetoresistance measurement.

(iii) Microscopic Technique.

2.5.1. Magnetization Curve:

Different types of techniques are available for the characterization of magnetization of the material. Hysteresis is well known in ferromagnetic materials. When an external magnetic field is applied to a ferromagnet, the atomic dipoles align themselves with the external field. Even when the external field is removed, part of the alignment will be retained: the material has become magnetize. Hysteresis phenomena occur in magnetic and ferromagnetic materials, as well as in the elastic, electric, and magnetic behavior of materials, in which a lag occurs between the application and the removal of a force or field and its subsequent effect. Electric hysteresis occurs when applying a varying electric field, elastic hysteresis occurs in response to a varying

force. If the displacement of a system with hysteresis is plotted on a graph against the applied force, the resulting curve is in the form of a loop. In contrast, the curve for a system without hysteresis is a single, not necessarily straight, line. Although the hysteresis loop depends on the material's physical properties, there is no complete theoretical description that explains the phenomenon. The family of hysteresis loop, from the results of different applied voltages and forces, form a closed space in three dimensions, called the hysteroid. If the magnetic field is now reduced linearly, the plotted relationship will follow a different curve back towards zero field strength at which point it will be offset from the original curve by an amount called the remanent flux density or "remanence".

If this relationship is plotted for all strengths of applied magnetic field the result is a sort of S-shaped loop. The 'thickness' of the middle bit of the S describes the amount of hysteresis, related to the "coercivity" of the material [36-38].

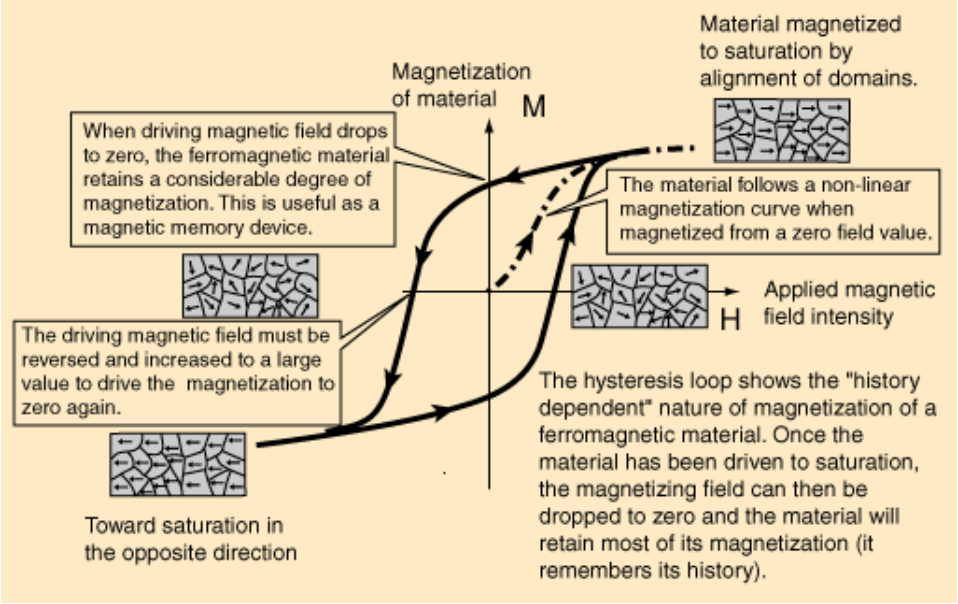

Fig (2.5): Different domain alignment in a hysteresis loop

When we apply an external field to a ferromagnet, equilibrium domain structure will be;

- The domains oriented most closely in the direction of the external field will gain in energy, the other ones loose; always following the basic equation for the energy of a dipole in a field.

- Minimizing the total energy of the system thus calls for increasing the size of favorably oriented domains and decreasing the size of unfavorably oriented ones. Stray field considerations still apply, but now we have an external field anyway and the stray field energy looses in importance.

- We must expect that the most favorably oriented domain will win for large external fields and all other domains will disappear.

- If we increase the external field beyond the point where we are left with only one domain, it may now even become favorable, to orient the atomic dipoles off their "easy" crystal direction and into the field.

- After that has happened, all atomic dipoles are in field direction - more we cannot do. The magnetization than reaches a saturation value that cannot be increased anymore.

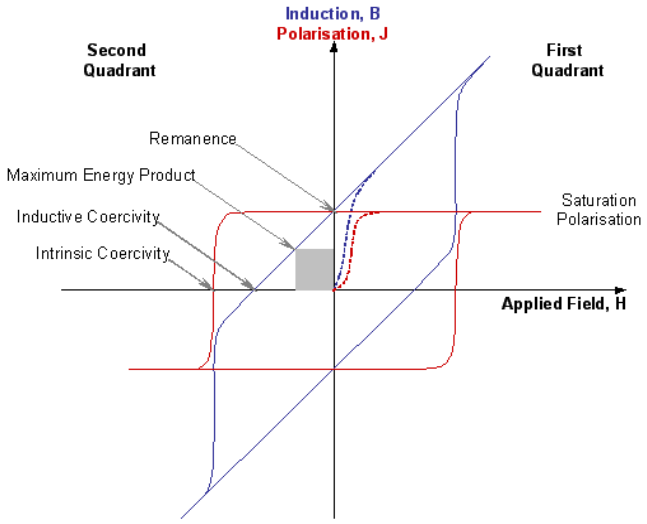

Fig (2.6): Different stages in the hysteresis loop.

2.5.1.1.Vibrating sample magnetometer (VSM):

Vibrating sample magnetometer or VSM is a scientific instrument that measures magnetic roperties. A sample is placed inside a uniform magnetic field to magnetize the sample. The sample is then physically vibrated sinusoidally, typically through the use of a piezoelectric material. Commercial systems use linear attenutators of some form and historically the

development of these systems was done using modified audio speakers, though this approached was dropped due to the interference through the in-phase magnetic noise produced, as the magnetic flux through a nearby pickup coil varies sinusoidally. The induced voltage in the pickup coil is proportional to the sample's magnetic moment, but does not depend on the strength of the applied magnetic field. In a typical setup, the induced voltage is measured through the use of a lock-in amplifier using the piezoelectric signal as its reference signal. By measuring in the field of an external electromagnet, it is possible to obtain the hysteresis curve of a material.

The principle of VSM is the measurement of the electromotive force induced by magnetic sample when it is vibrated at a constant frequency in the presence of a static and uniform magnetic field [39].

2.5.1.2.SQUID magnetometer:

superconducting quantum interference devices (SQUID), measure extremely small magnetic fields; they are very sensitive vector magnetometers, with noise levels as low as 3 $fT/Hz^{0.5}$ in commercial instruments and 0.4 $fT/Hz^{0.5}$ in experimental devices. Many liquid-helium-cooled commercial SQUIDs achieve a flat noise spectrum from near DC (less than 1 Hz) to tens of kiloHertz, making such devices ideal for time-domain biomagnetic signal measurements. By measuring the field, it is possible to obtain the hysteresis curve of the material [40, 41].

2.5.2. Magnetoresistance measurement:

Magnetoresistance is the property of a material to change the value of its electrical resistance when an external magnetic field is applied to it. The effect was first discovered by William Thomson (more commonly known as Lord Kelvin) in 1856, but he was unable to lower the electrical resistance of anything by more than 5%. This effect was later called ordinary magnetoresistance (OMR). More recent researchers discovered materials showing giant magnetoresistance (GMR), colossal magnetoresistance (CMR) and magnetic tunnel effect (TMR). When a magnetic field is applied in a direction perpendicular to the material, the resistance will be raised. This is called the magnetoresistance effect, and depends on the electron mobility of the material [42, 43]. MR was calculated by the following equation [44, 45]:

$$MR = \frac{\Delta R}{R0} = \frac{R(H) - R(0)}{R0} x100 \qquad (2.3)$$

Where, R (0) and R (H) are the resistance at zero and any applied field of H, respectively. The applied magnetic field is perpendicular to the film.

2.5.3. Microscopic Technique:

2.5.3.1.Lorentz Microscopy:

Lorentz microscopy has been used extensively for the past 40 years to study magnetic domain structure and magnetization reversal mechanisms in magnetic thin films and elements. In this chapter, the principal imaging and diffraction modes are reviewed, both qualitative and quantitative. In addition, a description of the instrumental and specimen requirements is included, and in the final section, the application of the various techniques to the study of spin-valve and spin-tunnel junction layered structures is discussed as a means of illustrating the type of information that can be obtained. Lorentz microscopy can play a valuable and often complementary role in characterizing the micromagnetic structure of ultrathin films and multilayers [46, 47].

2.5.3.2.Magnetic Force Microscopy:

Magnetic force microscope (MFM) is a variety of atomic force microscope, where a sharp magnetized tip is scanning the magnetic sample; the tip-sample magnetic interactions are detected and used to reconstruct the magnetic structure of the sample surface shown in the fig (2.7). Many kinds of magnetic interactions are measured by MFM, including magnetic dipole–dipole interaction. MFM scanning often uses non-contact AFM (NC-AFM) mode. The MFM can be used to image various magnetic structures including domain walls (Bloch and Neel), closure domains, recorded magnetic bits, etc. Furthermore, motion of domain wall can also be studied in an external magnetic field.

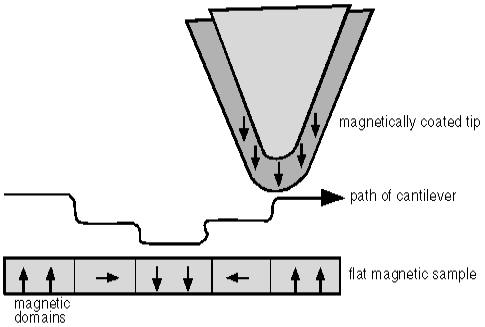

Fig (2.7): MFM Scanning principle

MFM images of various materials like thin films, nanoparticles, nanowires, permalloy disks and recording media [48, 49]. MFM is a powerful tool for high resolution magnetic imaging of most data storage media. As the density of magnetic media is higher, the bit become smaller than the wavelength of the light, so optical technique cannot resolve it. General MFM is capable of imaging the magnetic domain of several tens of nanometer. Also, MFM is almost simultaneous with measuring the surface characteristics of topography and roughness of the same area with sub-angstrong vertical resolution. MFM image is a magnetic stray field. MFM images are formed by scanning the attractive and repulsive magnetostatic field with the interactions between the shape of the magnetic tip in vertical direction and the surface of a sample in horizontal position. If magnetization of the sample is oriented along the vertical direction (z-axis) and the tip can be represented as a magnetic dipole with magnetization along the z-axis; the shifts are represented on MFM images by dark and bright regions, where the field is formed. So, large negative shifts (repulsion) are dark while large positive shifts (attraction) are bright [50, 51]. Three types of magnetic configurations can be identified by MFM: [52, 53].

(a) A light line separating two or more dark regions. This image can be assigned to multiple domains (MD) separated by a magnetic wall, MD configurations are dominant in the bigger structures.

(b) A bipolar image, consisting in contiguous bright and dark areas. This image is distinctive of single magnetic domains (SD). The bright and dark areas correspond to the magnetic field lines emerging from one pole and merging into the other. The SD configuration is characteristic of the smaller nuclei.

(c) A bipolar image showing a dark spot that forms in the light area. This kind of pseudosingle-domain (PSD) image has been rarely reported, and probably corresponds to a transitional structure. The PSD behavior is mostly observed in nuclei of intermediate size.

Principle of MFM:

In MFM, a tapping cantilever equipped with a special tip is first scanned over the surface of the sample to obtain topographic information. Using LiftMode as shown in Figure 2.8, the tip is then raised just above the sample surface. The surface topography is scanned while being monitored for the influence of magnetic forces. These influences are measured using the principle of force gradient detection. In the absence of magnetic forces, the cantilever has a resonant frequency f_0.

This frequency is shifted by an amount Δf proportional to vertical gradients in the magnetic forces on the tip. The shifts in resonant frequency tend to be very small, typically in the range 1-50 Hz for cantilevers having a resonant frequency f_0 ~100 kHz.

.

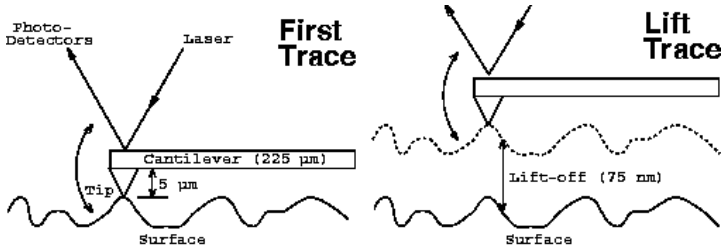

Fig (2.8): MFM LiftMode Principles

These frequency shifts can be detected three ways: phase detection, which measures the cantilever's phase of oscillation relative to the piezo drive; amplitude detection, which tracks variations in oscillation amplitude; and frequency modulation, which directly tracks shifts in resonant frequency. Phase detection and frequency modulation produce results that are generally superior to amplitude detection.

LiftMode allows the imaging of relatively weak but long-range magnetic interactions while minimizing the influence of topography (Figure 2.8). Measurements are taken in two passes across each scanline; each pass consists of one trace and one retrace. In the first pass, topographical data is taken in TappingMode on one trace and retrace. The tip is then raised to the lift scan height and a second trace and retrace performed while maintaining a constant separation between the tip and local surface topography. Magnetic interactions are detected during this second pass. Using LiftMode, topographical features are virtually absent from the MFM image.

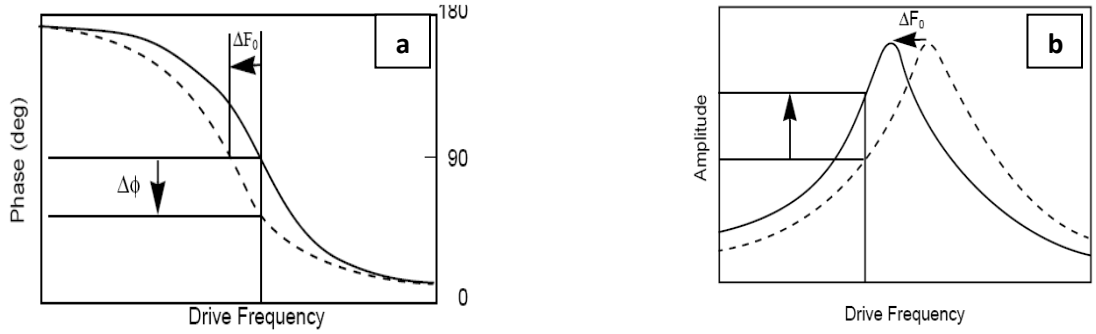

Fig (2.9): Different MFM modes

The phase curve should appear as in Figure (2.9 a), decreasing with increasing frequency, and crossing the center line (corresponding to a 90° phase lag) at the peak frequency. The phase curve then measures the phase lag between the drive voltage and the cantilever response. Again, vertical gradients in the magnetic force cause a shift Δf_0 in the resonance frequency. In this case, resonance shifts give rise to phase shifts $\Delta\varphi$ which then gives an image of the magnetic force gradients. As the tip oscillates above the sample, a gradient in the magnetic force will shift the resonance frequency f_0; (Figure 2.9 b). Tracking the variations in oscillation amplitude while in liftMode yields an image of the magnetic force gradients [54].

In MFM measurements, the magnetic force between the sample and the tip can be expressed as,

$$\vec{F} = \mu_o(\vec{m} \cdot \nabla)\vec{H}$$

Where $\vec{m}$ is the magnetic moment of the tip (approximated as a point dipole), $\vec{H}$ is the magnetic stray field from the sample surface, and μ_0 is the magnetic permeability of free space.

Since magnetic force is a long-range force, the tip volume strongly influences the tip–sample interaction of MFM. Figure 2.10 illustrates the schematics of the effect of geometry on interaction volume. A conventional large-volume tip can induce a large area of magnetic interaction. In contrast, a high aspect ratio (HAR) tip with a smaller cylindrical geometry can resolve a small area with a clearer image. Accordingly, a HAR tip coated with a thin magnetic film was prepared in this study to improve the MFM image resolution.

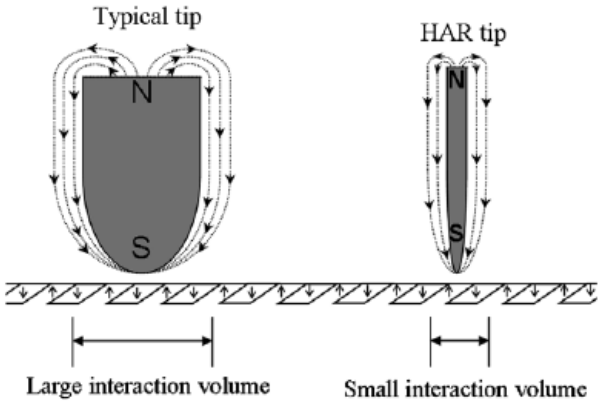

Fig (2.10): Schematic depiction of the effect of tip geometry on magnetic interaction volume. The dotted lines represent magnetic line of force of the magnetized tips. The arrows in the sample represent different magnetic domains

Scanning Procedure:

The scanning method when using an MFM is called the "lift height" method. When the tip scans the surface of a sample at close distances (< 100 nm), not only magnetic forces is sensed, but also atomic and electrostatic forces. The lift height method helps to enhance the magnetic contrast through the following:

- First, the topographic profile of each scan line is measured. That is, the tip is brought into a close proximity of the sample to take AFM measurements.
- The magnetized tip is then lifted further away from the sample.
- On the second pass, the magnetic signal is extracted.

2.6. Magnetic Thin film:

Thin films are thin material layers ranging from fractions of a nanometre (monolayer) to several micrometres in thickness. Electronic semiconductor devices, magnetic thin film materials and optical coatings are the main applications benefiting from thin film construction.

In recent years, thin films science has grown worldwide into a major research area. The importance of coating and the synthesis of new materials for industry have resulted in a tremendous increase of innovative thin film processing technologies. Currently this development goes hand in hand with the explosion of scientific and technological breakthrough in microelectronics, optics and nanotechnology. These films are essential for thermal barrier coating and wear protection, enhancing service life of tools and to protect materials against thermal and atmospheric influences. Therefore basic research activities will be necessary in the future to increase knowledge, understanding and develope predictive capabilities for relating fundamental physical and chemical properties to the microstructure and performance of thin films in various applications [55-57].

The greater field of magnetism is rich with thin film Phenomena. Thin films of magnetic material with thicknesses of a few nanometers to micrometer, are used in the electronics industry. Magnetic films can be single-crystal, polycrystalline, amorphous, or multilayered in the arrangement of their atoms. Applications include magneto-optic storage, inductive recording media, magnetoresist sensors, and thin-film heads [58, 59]. Nowadays,

magnetic nanostructures and spin electronic (spintronic) play a fundamental role in the development of upto- date professional and consumer technology. In particular, Magnetic Tunnelling Junctions (MTJs) are seen as one of the best candidate for the realization of non-volatile magnetic memories (MRAMs) and high-density data storage [60]. Cobalt and its alloys are widely used as typical magnetic materials applicable in various fields such as micro-electromechanical system (MEMS) devices, magnetic recording head, reading heads and data storage media [61]. Magnetic thin film heads are main parts of the hard disk drives that are employed as main data storage devices set in computer apparatus because of their large capacity, high data transfer rate and high reliability [62]. Development of a soft magnetic recording-head material with high saturation magnetic flux density (Bs) and low coercivity (Hc) is a prerequisite for realizing magnetic storage devices with a high areal recording density. Recently, many researchers have eagerly tried to prepare new soft magnetic materials to meet the demand for the rapidly increasing recording density [63]. Soft magnetic materials are a central component of electromagnetic devices such as step motors, magnetic sensors, transformers and magnetic recording heads [64]. Soft magnetic thin films are of great current interest because of their potential applications in a variety of micro magnetic devices including passive circuit elements, micromagnetic sensors, read/write heads for magnetic disk memories for computers, magnetic storage devices, etc. In thin films the magnetic properties can get influenced significantly by internal stresses generated during deposition as well as by surface irregularities. While internal stresses coupled with a non-zero magnetostriction may result in magnetic anisotropy. Surface irregularities may act as pinning centers for domain walls. Studies have shown that internal stresses in the film can significantly vary with film thickness [1]. Magnetic thin films are not only useful for practical applications such as magneto-optical recording but also important for the study of the inhomogeneous spin systems in low dimensions. The properties of magnetic films depend on the film thickness. The Curie temperature T_C, the value of the magnetization M, the orientation of the magnetic moments, etc. can depend drastically on the thickness and structure of the film [65]. Amorphous Co- and Fe-based soft magnetic thin films have received much attention due to their superior magnetic properties, such as high permeability, high saturation magnetization, low coercivity and low anisotropy field, leading to many applications in magnetic sensors and electromagnetic noise suppressors [66]. The magnetic properties of thin films vary with the deposition technique, temperature of deposition, as well as the choice of the

substrate because these conditions affect the film crystal orientation, structural quality, interface environment and interface sharpness. The interface anisotropy creates a strong dependence of the magnetic properties on the thickness of the magnetic layer which is the primary parameter used to control the magnetic properties of the films. Several previous studies indicated that one should not be too surprised to find that magnitude and sign of the magneto-elastic coupling coefficients differ substantially from their respective bulk values in the case of ultrathin and strained ferromagnetic films [67].

2.6.1. Deposition Techniques of Magnetic Thin film:

After discussing the magnetic thin films, this section is devoted to method/techniques by which films are deposited. The thin film process comprises three elementary stages including decomposition, transport, and nucleation and growth mechanisms. A number of processes are used for producing alloy thin films, multilayer thin film, necent metal thin films, and composites.

2.6.1.1.Vapour Phase Route:

These include lithography, vacuum deposition processes such as physical vapor deposition (PVD) and chemical vapor deposition (CVD), and spray coatings. Gaseous phase processes are based on evaporation and nucleation phenomena. Nucleation involves conversion from a vapour phase to a particulate phase [68-70].

2.6.1.2.Solid phase Route:

These include milling by ball mill, planetary mills, attrition mills, vibratory mills etc. The advantages of these techniques are that they are simple, require low-cost equipment and, provided that a coarse feedstock powder can be made, the powder can be processed. However, there can be difficulties such as agglomeration of the powders, broad particle size distributions, contamination from the process equipment itself, and often difficulty in getting to the very fine particle sizes with viable yields. It is commonly used for inorganic and metals, but not organic materials [71].

2.6.1.3.Liquid phase Route:

This includes electrochemical deposition, sonoelectrochemical deposition where power ultrasound is irradiated to the electrodepositing bath.

2.6.1.4.Electrochemical deposition:

Electrodeposition (ED) on the other hand is a well established technology, which can be a complement to the more expensive high vacuum methods. Electrodeposition is a useful

technique to deposit different metals and alloys. In most cases, these materials are fabricated by vacuum deposition, sputtering, sol–gel, spray pyrolysis, etc. All these methods require a high degree of process control, which could be accomplished only with the use of expensive equipment and involve a huge wastage of materials. Preparation of thin film of alloy and multilayer materials by electrodeposition technique has received much interest in recent years and they have been utilized for a variety of applications such as magnetic materials, noble metal catalysts, etc. Electrodeposition is a very simple and cost-effective fabrication process. It has the advantage of preparing films over a large surface area in a relatively shorter period without sacrificing the materials purity [72]. Electroless deposition has been used extensively to produce the well known and widely used amorphous Ni-P alloys. The method of electrodeposition provides a very cost- and time-efficient way of growing ultrathin films on large area substrates. Despite these advantages, it is not yet widely used for the preparation of magnetic thin film systems. One reason is that the electrochemically grown multilayers do not exhibit the high GMR effects of systems prepared by physical methods, which is mainly related to differences in their microstructure. There is a considerable lack of understanding of the microscopic processes of growth and their influence on the magnetic and electrical transport properties [73]. Electrodeposition is used to produce materials and architectures that cannot be built by traditional techniques. By means of this method, different materials, such as nano/micrometer-scale crystallites, nanocomposites, epitaxially deposited metal films and ceramic materials have been prepared. Electrodeposition is an intrinsically fast technique which is compatible with patterning and large scale production [74]. Electrodeposition remains comparatively more empirical even though an atomic view of the process has now emerged. In electrodeposition the metal species are dissolved in solution in the form of solvated cations or complexes. Metal phase formation requires reducing them by transfer of electrons from the substrate according to the reaction $M^{Z+} + ze = M$ which standard redox potential is $E_0 = E (M^{Z+}/M)$. For convenience, one often defines the deposition overpotential $\eta = E_0\text{-}U$: electrodeposition requires therefore applying $\eta > 0$ or an electrode potential U smaller than E_0. In some instances under potential deposition (UPD) is observed, i.e. deposition occurs for $\eta < 0$. The UPD process resembles an adsorption stage with the formation of a uniform monolayer composed of metal adatoms and anions. This phenomenon is the archetype of a surface-limited reaction. It is sensitive to the nature of the anions and in some instance a specific anion may induce UPD. Electrodeposition is also suitable

to deposit various epitaxial oxide layers ZnO and II–VI semiconductors with excellent electronic and optical properties [75]. The underpotential deposition (upd) process, is known as the phenomenon in which up to a monolayer of metal deposits onto a foreign metal substrate (usually the electrode) at potentials positive from the reversible Nernst potential due to distinct interaction between them. The underpotential deposition of a metal can form on the electrode surface a metallic layer that shows high catalytic activity towards several electrodic processes [76]. Electrochemically formed aluminum oxide films were initially selected for these studies as they have a well-known porous structure, with pores of controllable distribution and dimensions [77]. Electrochemical processing with using nanoporous templates allows us to prepare metallic nanowire arrays with various controlled dimensions. The ability to control the composition along the length of the nanowire is an important feature of the electrochemical method. Understanding of the coupling between ionic mass transport phenomena and morphological variation within nanoscopic pores is indispensable to allow a more quantitative control of nanoscale materials formed by the electrochemical method. Especially, the control of nucleation and growth is expected to be widely applicable to the advanced designs and thus necessary. Solution phase synthesis of nanoparticles is one example pointing out the importance of the above respect. Growth model for electrochemical nucleation and growth were initially developed in the 1980s. Scharifker and Hills proposed the models for a diffusion-limited process, based on analysis of the current transient characteristic in the early stages of electrodeposition [78]. It is generally found that electrodeposition on semiconductors starts from surface defects and the growth itself follows a Volmer–Weber mode. Direct electroplating of ferromagnetic transition metal thin films onto silicon, in special Fe, is intrinsically complex due to the mutual chemical reactivity and local pH fluctuations with hydrogen bubbles generating on the working electrodes. Recently, different groups demonstrated that plating solutions alternative to a Watts bath conventional consisting of metal sulphate/ chloride with pH-controlling agent by boric acid, can be used to grow Nickel thin films and nanostructures onto graphite electrodes [79].

The electrodeposition of metals, described by a process of nucleation followed by diffusion limited three dimensional growths, is an area of considerable interest. Modelling of deposition potentiostatic current transients is an informative method of analysis, potentially revealing parameters such as the nucleation rate, saturation nucleus density, and number of active sites [80].

Scharifker and Hills [81] developed a theoretical model to analyze the current–time transient results of chronoamperometric experiments. In their models, two limiting nucleation mechanisms, i.e., instantaneous nucleation and progressive nucleation were considered. Instantaneous nucleation corresponds to immediate activation of all nucleation sites, so that the rate of further nuclei formation is negligible and nuclei growth is slow in the time frame of the experiments. For progressive nucleation, the rate of new nuclei formation is not negligible and the growth of nuclei is fast, which will produce different sizes of nuclei during nucleation. The models for instantaneous and progressive nucleation, followed by three-dimensional diffusion-limited growth, are given by Eqs. (2.4) and (2.5), respectively:

$$I=\frac{ZCFD^{1/2}}{\pi^{1/2}t^{1/2}}[1-\exp(-N\pi kDt)] \qquad (2.4)$$

$$I=\frac{ZFCD^{1/2}}{\pi^{1/2}t^{1/2}}\left[1-\exp\left(\frac{-AN_0\pi k'Dt^2}{2}\right)\right] \qquad (2.5)$$

The theoretical values for the gradient of rising portion of an Instantaneus nucleation and progressive nucleation are 0.5 and 1.5 respectively.

CHAPTER -3

Experimentation

Experimental Setup
Electrolytic bath preparation
Cyclic Voltammetry
Chronoamperometry
X-Ray diffraction (XRD)
Scanning Electron Microscope (SEM)
Magnetic force microscope (MFM)

3.1. Experimental Setup:

Electrochemical studies or experiments were conducted with a potentiostat/galvenostate (Eco Chemie Netherland, Autolab PGSTAT 12) system having computer interface of GPES software and three electrodes electrochemical cell. Experiments were performed on graphite (Asbury) substrates of exposed surface area of 0.25 cm × 0.25 cm. A graphite plate 1 cm breadth and an Ag/AgCl electrode (Eco Chemie, Netherlands) served as counter and reference electrodes respectively. Before each scan and subsequent experiment, electrodes were polished, washed and dried properly. The temperature of electrolyte solution was measured with digital thermometer. Fig (3.1) is an experimental arrangement of electrolytic bath preparation of metal and alloy deposition.

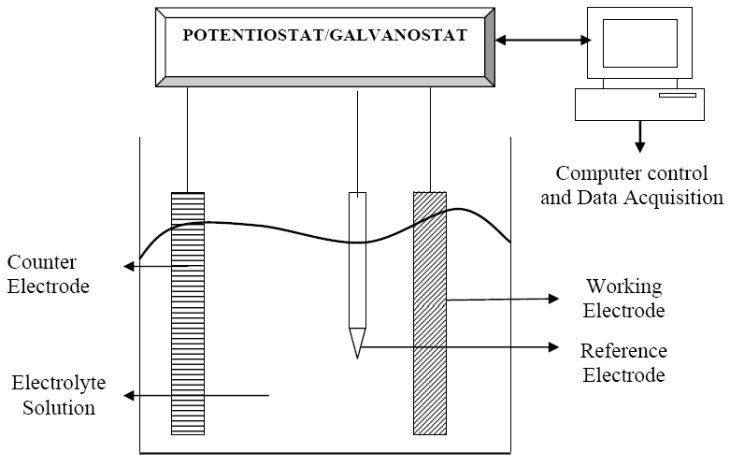

Figure 3.1 Schematic of a standard three-electrode cell.

3.2. Electrolytic bath Preparation:

The plating bath contains metallic salts used for making solution conductive. All chemicals were from commercial sources and were the highest purity available. They were used without further purification. Solution was prepared from an additive free chemical bath in doubly distilled water at room temperature and under moderate agitation. All solutions in this study were prepared from doubly distilled water. Different types of alloy thin film and the corresponding necent metals are deposited. The concentration of the bath for different metals and alloy deposition are given in the table below (Table 3.1).

TABLE-3.1: Concentration of the bath:

Types of Thin Film	Chemicals Used						
	$CuSO_4.5H_2O$	$CoSO_4.7H_2O$	$NiSO_4.6H_2O$	$NiCl_2.6H_2O$	H_3BO_3	H_2SO_4	Na_2SO_4
Cu	**0.04M**	**-**	**-**	**-**	**-**	**40gpl**	**-**
Co	**-**	**0.5M**	**-**	**-**	**-**	**-**	**0.25M**
Ni	**-**	**-**	**0.76M**	**0.15M**	**0.37M**	**-**	**-**
Co-Cu alloy	**0.04M**	**0.5M**	**-**	**-**	**0.25M**	**-**	**-**
	0.03M	**0.5M**	**-**	**-**	**0.25M**	**-**	**-**
	0.02M	**0.5M**	**-**	**-**	**0.25M**	**-**	**-**
Ni-Cu alloy	**0.009M**	**-**	**0.175M**	**-**	**0.46M**	**-**	**-**
	0.012M	**-**	**0.175M**	**-**	**0.46M**	**-**	**-**
	0.015M	**-**	**0.175M**	**-**	**0.46M**	**-**	**-**

3.3. Synthesis:

Electrodeposition is used as a route to fabricate magnetic alloy thin film as well as corresponding metal thin film. The deposition was commenced in potentiostatic mode. The laboratory setup for electrodeposition has an electrolytic bath maintained at a particular composition with cathode and anode immersed in the bath. Temperature is maintained at 25°C. The key variables of the electrodeposition include deposition potential of the bath and Cu concentration for the alloy deposition. And the key variables of the electrodeposition for the nascent metal include only the deposition potential.

3.4. Electrochemical Analysis:

The electrochemical phase formation is studied by methods including cyclic voltammetry (CV) and Chronoamperometry (CA). Here the basic principles underlying CV and CA are described, as they have been used in the analysis and synthesis of the copper thin films.

3.4.1. Cyclic Voltammetry:

Electrochemical deposition of metals and metal oxides typically proceeds by oxidation or reduction of species in a solution. Cyclic voltammetry is an attractive method for teaching a number of concepts in electrochemistry. Cyclic voltammetry is a very versatile electrochemical technique which allows probing the mechanics of redox and transport properties of a system in solution. This is accomplished with a three electrode arrangement whereby the potential relative

to some reference electrode is scanned at a working electrode while the resulting current flowing through a counter (or auxiliary) electrode is monitored in a quiescent solution

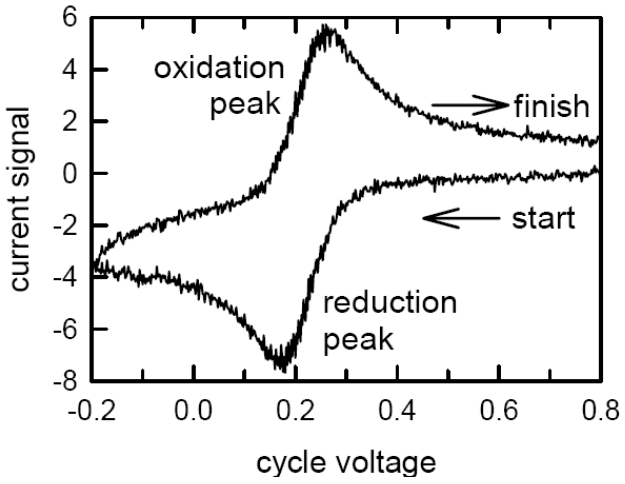

Fig (3.2): A typical cyclic voltammogram showing reduction and oxidation current peaks.

In typical cyclic voltammetry, a solution component is electrolyzed (oxidized or reduced) by placing the solution in contact with an electrode surface, and then making that surface sufficiently positive or negative in voltage to force electron transfer. In simple cases, the surface is started at a particular voltage with respect to a reference half-cell such as calomel or Ag/AgCl, the electrode voltage is changed to a higher or lower voltage at a linear rate, and finally, the voltage is changed back to the original value at the same linear rate. When the surface becomes sufficiently negative or positive, a solution species may gain electrons from the surface or transfer electrons to the surface. This results in a measurable current in the electrode circuitry. However, if the solution is not mixed, the concentration of transferring species near the surface drops, and the electrolysis current then falls off. When the voltage cycle is reversed, it is often the case that electron transfer between electrode and chemical species will also be reversed, leading to an "inverse" current peak. These features are illustrated in Figure 3.2 [82].

3.4.2. Chronoamperometry:

Chronoamperometry (CA) is an electrochemical method in which a step potential is applied and the current, i, is measured as a function of time, t. This i-t response is comprised of two components: the current due to charging the double-layer and the other due to the electron transfer reaction with the electroactive species. Of course, the extent to which both occur simultaneously depends on the initial, E_i, and the final value, E_f, of the potential. The results are most easily interpreted when a planar (flat) electrode is used in a quiet, unstirred solution, and

the applied potential is sufficient to reduce or oxidize the electroactive species as fast as it gets to the electrode surface, i.e., at a diffusion-controlled rate.

In chronoamperometry, the working electrode potential is suddenly stepped from an initial potential to a final potential, and the step usually crosses the formal potential of the analyte. The solution is not stirred. The initial potential is chosen so that no current flows (i.e., the electrode is held at a potential that neither oxidizes nor reduces the predominant form of the analyte). Then, the potential is stepped to a potential that either oxidizes or reduces the analyte, and a current begins to flow at the electrode. This current is quite large at first, but it rapidly decays as the analyte near the electrode is consumed, and a transient signal is observed. If the point in time when the potential is stepped is taken as time zero, then the Cottrell equation describes the how the current, I, decays as a function of time, t as shown in the fig 3.3.

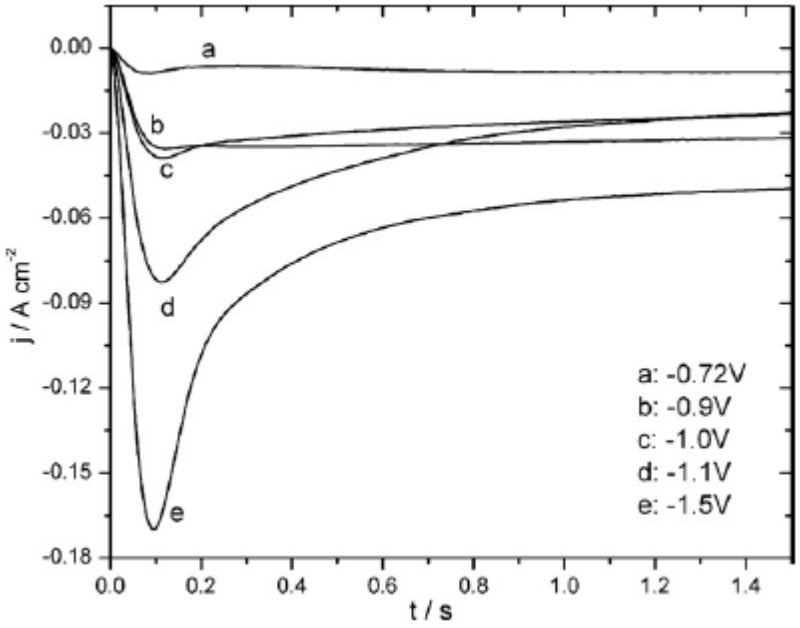

Fig (3.3): Chronoamperometry (Current-time transient) Curve

Current, i, vs. time t, response in the presence of an electroactive species that undergoes an electron transfer reaction at a diffusion-controlled rate. Under these conditions, the current decay is given by,

$$i = \frac{nFAD^{1/2}C^{b}}{(\pi t)^{1/2}} \qquad (3.1)$$

Where n is the number of electron(s) transferred per electroactive molecule or ion; F is Faraday's constant; A is the area of the electrode surface in cm^2; D is the diffusion coefficient in cm^2/s; C^b

is the concentration of the electroactive species in mol/cm^3; and t is time in second. The current raises rapidly to a maximum value decays as a function of $t^{1/2}$, as seen in figure (83, 84).

3.5. Characterization Technique:

Several techniques have been used to characterize the electrodeposits of thin film. Details of the techniques are enlisted below. Magnetic force microscopes (MFM) were employed to examine the morphology, particle size and microstructure of the electrodeposits of thin film at the various potential and Cu concentration. The chemical composition/purity of the electrodeposits was determined by energy dispersive spectroscopy (EDS) analysis. Schrifkar and Hills model of nucleation and growth are used to study the nucleation and growth mechanism.

3.5.1. X-Ray Diffraction (XRD):

The X-ray diffraction, in the range of scanning angel 40-110° and 40-120° at a scanning rate 2° with CuKα radiation (λ=1.5406A0) using Philips X' PERT System X-Ray Diffractometer. X-ray scattering techniques are a family of non-destructive analytical techniques which reveal information about the crystallographic structure, chemical composition, and physical properties of materials and thin films. X-ray diffraction line profile analysis is an adopted technique, powerful tool and non-destructive method, to characterize the behavior of different materials.

XRD techniques are based on the elastic scattering of X-rays from structures that have long range order. XRD is a technique used to characterise the crystallographic structure, crystallite size (grain size), and preferred orientation in polycrystalline or powdered solid samples. An effect of the finite crystallite sizes is seen as a broadening of the peaks and strain in an X-ray diffraction as is explained by the Williamson-Hall formula [85].

3.5.2. Scanning Electron Microscope (SEM):

To characterize the sample morphology, JEOL-JSM 6480LV Scanning Electron Microscope (SEM) at low acceleration voltages is used. The Scanning electron microscope (SEM) is a type of electron microscope that images the sample surface by scanning it with a high-energy beam of electrons in a raster scan pattern. The electrons interact with the atoms that make up the sample producing signals that contain information about the sample's surface topography, composition and other properties such as electrical conductivity. The types of signals produced by an SEM include secondary electrons, back-scattered electrons (BSE), characteristic X-rays, light

(cathodoluminescence), specimen current and transmitted electrons. The signals result from interactions of the electron beam with atoms at or near the surface of the sample. Back-scattered electrons (BSE) are beam electrons that are reflected from the sample by elastic scattering. Characteristic X-rays are emitted when the electron beam removes an inner shell electron from the sample, causing a higher energy electron to fill the shell and release energy. These characteristic X-rays are used to identify the composition and measure the abundance of elements in the sample. Energy dispersive X-ray spectroscopy (EDS or EDX) is an analytical technique used for the elemental analysis or chemical characterization of a sample. The incident beam may excite an electron in an inner shell, ejecting it from the shell while creating an electron hole where the electron was. An electron from an outer, higher-energy shell then fills the hole, and the difference in energy between the higher-energy shell and the lower energy shell may be released in the form of an X-ray. The number and energy of the X-rays emitted from a specimen can be measured by an energy dispersive spectrometer [86, 87].

3.5.3. Magnetic Force Microscope (MFM):

The surface topology and magnetic measurement was taken by an SPM lab-programmed Veeco dilnnova Magnetic force microscope (MFM) in tapping mode at a lift height of 50nm and a Sb(n) doper Si tip coated with Co/Cr/BOT -1-10 nm Cr on both sides. Magnetic force microscope (MFM) is a variety of atomic force microscope, where a sharp magnetized tip is scanning the magnetic sample; the tip-sample magnetic interactions are detected and used to reconstruct the magnetic structure of the sample surface. Many kinds of magnetic interactions are measured by MFM, including magnetic dipole–dipole interaction. MFM scanning often uses non-contact AFM (NC-AFM) mode. Because the stray magnetic field from the sample can affect the magnetic state of the tip, and vice versa, interpretation of the MFM measurement is not straightforward. For instance, the geometry of the tip magnetization must be known for quantitative analysis. Typical resolution of 30 nm can be achieved, although resolutions as low as 10 to 20 nm are attainable [88].

CHAPTER -4

Results & Discussion

Cu, Cu & Ni thin film
Electrochemical analysis (Cyclic voltammetry, Chronoamperometry)
Characterization (XRD, SEM & MFM)
Cu-Co & Ni-Cu magnetic alloy thin film
Electrochemical analysis (Cyclic voltammetry, Chronoamperometry)
Characterization (XRD, SEM & MFM)

4.1. Copper, Nickel and Cobalt Thin film:

4.1.1. Cyclic Voltammetry:

Cyclic voltammetry (CV) of Cu was performed in the [-0.6 to 0.6] V potential range to identify the presence of the electrodeposition processes and to verify the electrochemical behavior of the electrodes in the elctrodeposition bath. Figure 4.1 (a) shows typical CV for graphite electrodes obtained with a scan rate of 10 mV/sec. Voltammogram is characterized by the presence of cathodic-anodic peaks associated with deposition and dissolution of Cu. Furthermore, in the curve, it is possible to note the presence of crossovers of the cathodic and anodic branches, typical of the formation of a new phase, involving a nucleation followed by diffusion limited growth process.

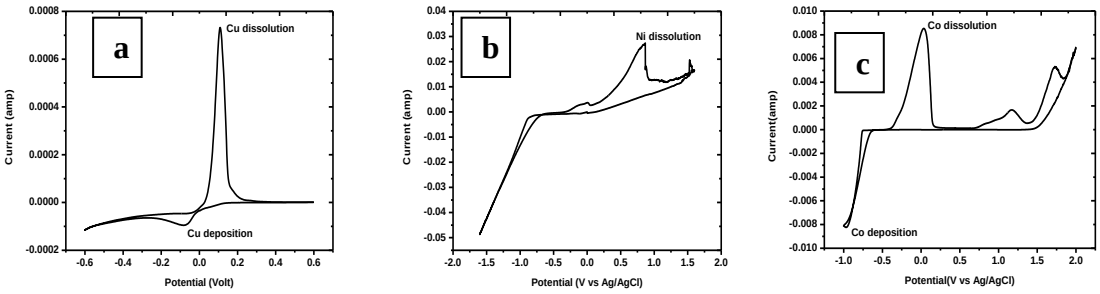

Fig (4.1): Cyclic voltammetry of (a) Cu, (b) Ni, (c) Co deposition on graphite at a scan rate of 10 mV/s at 25°C

From the Fig 4.1(a), beginning of current decrease was detected at –0.001 V vs. Ag/AgCl. It is clear from the voltammogram that a sharp rising cathodic current is observed as the potential is swept to –0.080 V which is the deposition peak of Copper. On reversing the scan direction, metal already deposited on the electrode surface continues to grow as a result of the Cu^{2+} (aq) $+2e^{-}$ = (s) reaction remaining thermodynamically and kinetically favorable. Sharp anodic peaks are observed when the potential is swept in positive direction and form the anodic peak at 0.107V Vs SCE, which is the dissolution peak. The key features of the Cu voltammogram are given in the Table-4.1. To analyze the cathodic efficiency of copper deposition, the charge due to cathodic (Qc) and anodic (Qa) processes can be obtained from integration of the cathodic and anodic branches of the I-E curves. The Qa/Qc ratio for the Cu deposition from the solution is

found to be 0.77. This indicates that Cu deposited during the cathodic sweep potential is not totally oxidized during anodic scan.

Table-4.1: Key feature of CV of Cu, Ni and Co deposition:

Items	Values		
	Cu	**Ni**	**Co**
Cathode depositing peak potential/V	-0.080	-	-
Anodic stripping peak potential/V	0.107	0.859	0.032
Cathode depositing peak height/A	-5.18×10^{-5}	-	-
Anode stripping peak height/A	7.65×10^{-4}	1.608×10^{-2}	8.481×10^{-3}
Cathode depositing peak area/C	8.22×10^{-4}	-	-
Anode Stripping peak area/C	5.87×10^{-3}	3.999×10^{-1}	2.290×10^{-1}

For Ni deposition, CV was performed in a scan range from -1.6 to 1.6 V at a scan rate of 10mV/Sec at 25°C. Fig 4.1 (b), shows the cyclic voltammogram of Ni in watt's bath. There is no remarkable reduction peak. On reversing the scan direction, metal already deposited on the electrode surface continues to grow as a result of the Ni^{2+} (aq) $+2e^{-}$ = Ni (s) reaction remaining thermodynamically and kinetically favorable. Sharp anodic peaks are observed when the potential is swept in positive direction and form the anodic peak at 0.859V Vs SCE, which is the dissolution peak. The crossover potential is at 0.72V vs SCE. The presence of crossover potential indicates the nucleation is diffusion controlled phenomena. The dissolution peak is found at 0.859V vs SCE. The presence of crossover is diagnostic for diffusion controlled phenomena. The crossover potential is -0.72V vs SCE. The cathode efficiency of Ni deposition is 0.26. The key features of the Ni obtained from the CV of Ni are given in the Table 4.1.

Fig 4.1(c) shows the CV of Co deposition. From the Fig, beginning of current decrease was detected at –0.61 V vs. Ag/AgCl. It is clear from the voltammogram that a sharp rising cathodic current is observed as the potential is swept to –0.96 V which is the deposition peak of Cobalt.

On reversing the scan direction, metal already deposited on the electrode surface continues to grow as a result of the $Co^{2+}+2e^{-} \rightarrow Co(s)$ reaction remaining thermodynamically and kinetically favorable. Sharp anodic peaks are observed when the potential is swept in positive direction and form the anodic peak at 0.032 V Vs SCE, which is the dissolution peak. Here also crossover is detetected at a potential -0.62V vs SCE. The cathodic efficiency of Co is found to be 1.22. This over efficiency is indicating other reaction at the electrode surface, which is also confirmed from the figure where another two anodic peak is observed, may be due to oxygen evolution.

4.1.2. Chronoamperometry:

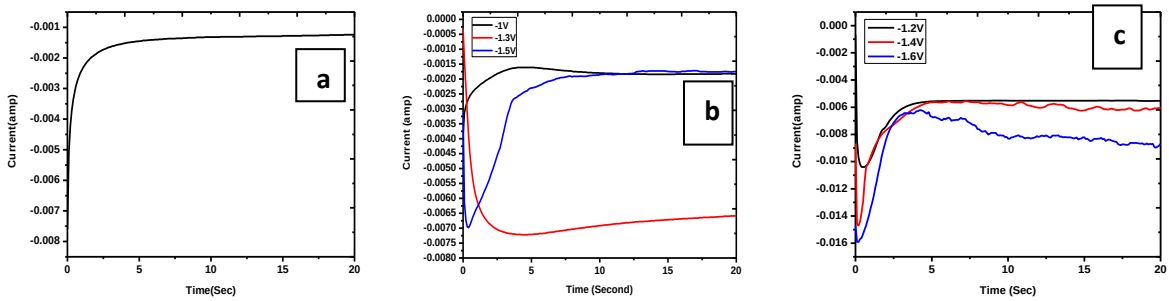

Fig(4.2): Chronoamperometry of (a) Cu, (b) Ni, (c) Co at diffent deposition potential at 25°C

Fig (4.2) shows the chronoamperogram of Cu, Ni and Co at different deposition potential at 25°C. Chronoamperometry was used to study the electrodeposition mechanism of different metal on the graphite cathode. In Fig 4.2(a), the deposition is done at -1.2V for 20 minute duration. The current transient curve gradually increases, indicating only the nucleation of Cu crystallites. In Fig 4.2 (b), for Ni the deposition is done at -1V, -1.3V and -1.5V for 20 seconds. For -1.3V and -1.5V, the general shape of the curves in Fig. 4.2(b) is due to the fact that initial nucleation results in a rapid increase in reduction current. Ion reduction occurs more rapidly than ion diffusion to the surface, resulting in a depletion of ion concentration near the surface. This then leads to a decrease in reduction current until a steady state is achieved at longer deposition time for -1.3V and shorter time for -1.5V. But in case of -1V, the nucleation becomes very less, the curve shows the growth of the nuclei. In the Fig 4.2(c), for Cobalt deposition, the current transient shows the nucleation and growth mechanism of the Co nuclei. There is a significant increase in the maximum reduction current observed with increasing negative overpotential in the electrodepositing bath. Hence, the results signify nucleation time was shorter for high negative

potential. This may be an indication of better deposit at higher deposition potential. For all the Cu, Ni, and Co deposits, the method relies on determining the gradient of a region of the log (current) Vs log (time) plot corresponding to the rising section of the transient plot. The slope of log (current) Vs log (time) varied from 0.1 to 0.6, which indicates instantaneous nucleation process for all the deposition kinds. The kinetic parameters calculate from the current transient is shown in the Table 4.2.

Table 4.2: Calculated Kinetic Parameter of Cu, Ni and Co deposits:

Material	**Potential (volt)**	**I_{max} (10^{-2} A/cm)**	**T_{max} (S)**	**D × 10^{-14} (cm^2 s^{-1})**	**N×10^{14} (cm^{-2})**	**Q (C)**
Cu	-1.2	-0.21	19.1	1.52	0.015	0.76
	-1	-0.16	3.98	0.50	0.0186	0.03
Ni	-1.3	-0.72	4.00	1.25	0.0007	0.13
	-1.5	-0.69	0.39	1.01	0.1051	0.05
	-1.2	-0.10	0.48	0.91	0.0032	0.12
Co	-1.4	-0.14	0.21	0.08	0.0094	0.28
	-1.6	-0.19	0.12	0.08	0.0013	0.21

4.1.3. XRD Analysis:

Structural analysis of the deposits was performed using XRD. Fig 4.3 shows X-ray diffraction pattern of different metals deposited on graphite substrate in the range of scanning angel 40-110° and 40-120° at a scanning rate 2° with CuKα radiation (λ=1.5406A0) using Philips X' PERT System X-Ray Diffractometer. The XRD patterns of the samples synthesized at different deposition potential are as shown in Fig 4.3. Decrease in either domain size or lattice strain will cause effective broadening of diffracted peaks. Average crystallite sizes of the deposit were determined by the Williamson–Hall formula (as Scherrer equation is valid only for powders or loosely bound deposits but not for hard and adherent deposits). The contribution of the particle size and nonuniform strain in the grains to the observed X-ray line broadening, β, are considered to be additive generating the formula as:

$$\beta_{total}=\beta_{particle}+\beta_{strain}=\frac{(0.94)\lambda}{tCos\theta}+4tan\theta\frac{\Delta d}{d} \quad (4.1)$$

The total broadening (βtotal) is the measured FWHM in radians, corrected for instrumental broadening. The X-ray wavelength of the source Cu Kα is λ=0.15418 nm, where t is the particle size, and 4 (Δd/d) represents the strain. Multiplying both sides of the equation by cos θ gives the final form, β_{total} cos θ=0.94λ/t+4 sin θ (Δd/d), which is used to calculate the particle size and lattice strain of the different metal deposit from the plot of β_{total} cos θ versus sin θ. The obtained grain size variation is given in Table 3.3.

Table 4.3: Crystallite size and lattice strain of of Cu, Ni & Co deposits:

Materials	Potential (Volt)	Crystallite size (nm)	Strain (%)
Cu	-1.2	224	0.004
	-1	131	0.005
Ni	-1.3	60	0.002
	-1.5	26	0.032
	-1.2	210	0.007
Co	-1.4	187	0.004
	-1.6	122	0.001

From the fig 4.3(a), one main peaks of Cu at 2θ = 43.47° is attributed to the (111) being the most intense is detected. As the film thickness are below 1 μm, the X-ray beams might have penetrated to the surface more pass the coating resulting the carbon identification and not the pure copper. The crystallite size and lattice strain of Cu at -1.2V is shown in the table above. In fig 4.3(b), two main peak of Cobalt at 44.37° and 84.10° are attributed to (002) and (103) respectively for all deposition potential. The crystallite size and lattice strain are shown in the table 3.3. Here we can see as the deposition potential is increases the crystallite size decreases and strain increases. This shows the effective broadening in the diffracted peaks. In fig 4.3(c), there are two Ni peaks are identified at 2θ=44.23° and 78.82° and attributed as (112) and (101) repectively. Table shows the crystallite size decreases and lattice stain increase with increasing deposition potential.

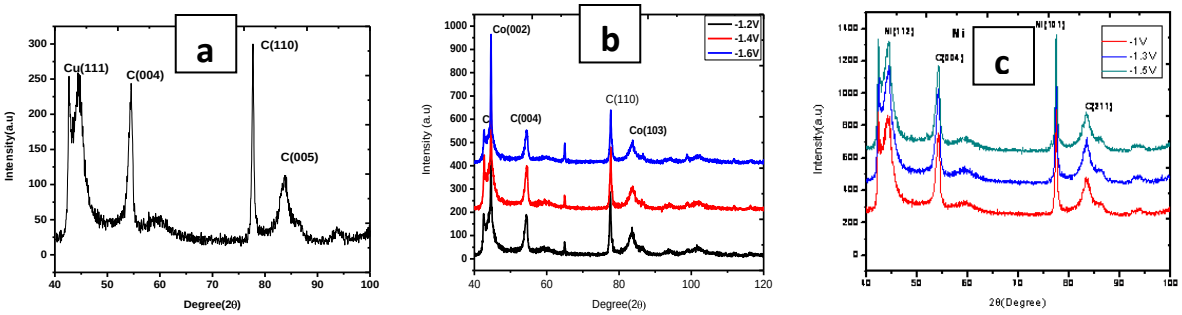

Fig(4.3): XRD of (a) Cu (b) Co (c) Ni at different deposition potential at 25°C

4.1.4. SEM (Morphology) Analysis:

Film morphology and composition is obtained by JEOL 6480 LV scanning electron microscope (SEM) at low acceleration voltages. In the fig 4.4, Cobalt morphology is shown as a function of deposition potential. At -1.2V, film consists of spherical particle. As deposition potential increases the morphology of the particles changed from spherical to dendritic structure. At -1.4V, the surface coverage is more and uniformly distributed on the substrate. At this potential, both the structure is present.

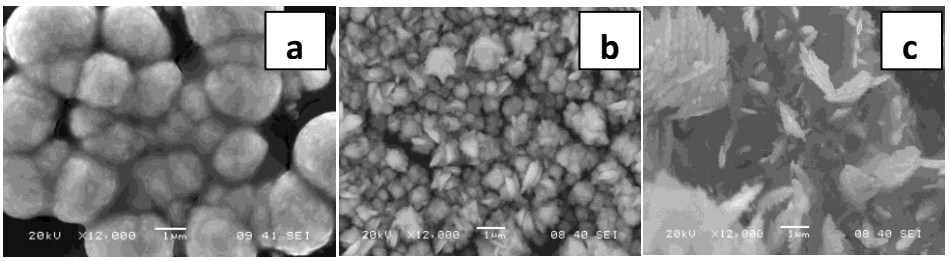

Fig (4.4): SEM of Co at (a)-1.2V, (b) -1.4V, (c) -1.6V at 25°C

Fig (4.5) shows, the film morphology of Nickel at different deposition potential on the graphite substrate at25°C. Here we can see as the deposition potential increases the surface coverage is more and also grain size is reduced, which is also calculated from XRD pattern. At -1.5V some secondary nuclei are formed on the surface. The basic characteristic of morphology is a uniform Nickel covered surface with well agglomerated spheroids. Above result is attributed to the following facts. First, temperature has resulted high supersaturation favoring formation of smaller nuclei but in a random fashion of discharging. Second**,** deposition potential has helped in rate of mass transportation thus creating enhanced nucleation. This effect has filled the gap between two adjacent nuclei leading to a compact mass.

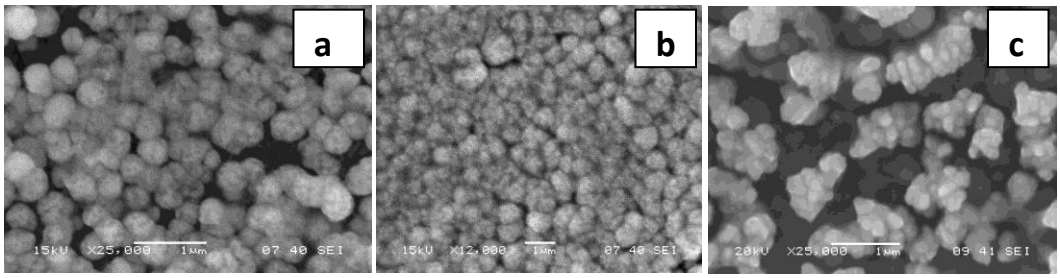

Fig (4.5): SEM of Ni at (a) -1V (b) -1.3V, (c) -1.5V at 25°C

Fig (4.6) shows the morphology of Copper deposits on the graphite electrode at -1.2V. Figure shows the well agglomerated spherical Cu particles with high surface coverage.

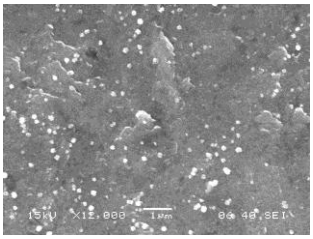

Fig (4.6): SEM of Cu at -1.2V at 25°C

4.1.5. MFM (Magnetic) Characterization:

The surface topology and magnetic measurement was taken by an SPM lab-programmed Veeco dilnnova Magnetic force microscope (MFM) in tapping mode at a lift height of 50nm and a Sb(n) doper Si tip coated with Co/Cr/BOT -1-10 nm Cr on both sides.

Fig (4.7) shows the MFM topography and magnetic phase image of Cobalt at -1.2V. The surface average roughness (Ra) of the Co deposit is found to be 713 nm. The topographic figure indicates the presence of aggregates of different sizes on the electrode surface. For Cobalt deposition, the magnetic force derivative was assessed through the phase variation. The magnetic phase images can characterize the presence or absence of magnetic phases with the domain orientations. The light colour in magnetic phase image would seem to indicate the presence of strong field emanating from the graphite substrate.

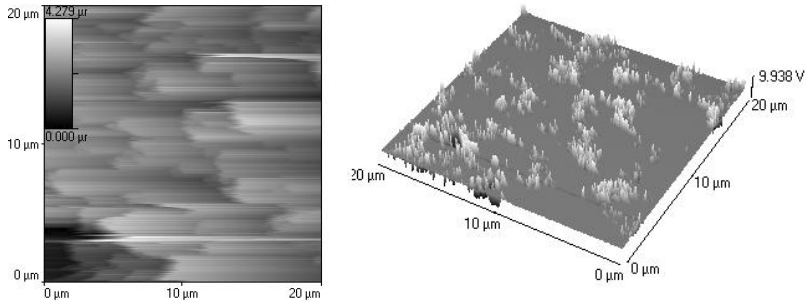

Fig(4.7): MFM of Co at -1.2V (a) Topograph, (b) Magnetic Phase

Fig (4.8) shows the topographic and magnetic images at different modes. The average roughness of the Cu film is found to be 563 nm. As Cu is a diamagnetic material, when the magnetized tip of the MFM scans the surface of the film, it cannot create the magnetic stray field. So maximum area of the image is grey, indicating the presence of the non magnetic material.Some of the areas is dark that may be due to the impurity deposition, along with the Cu deposition. In fig 3.15(c), TM deflection mode also showing, the irregularities in the alignment of the domain structure.

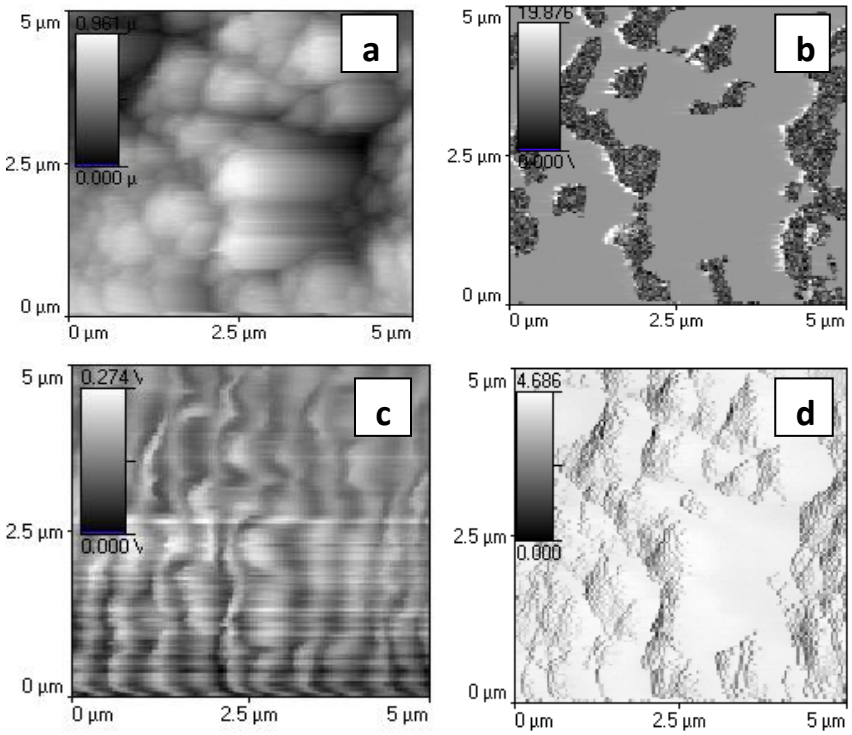

Fig(4.8): MFM of Cu at -1.2V (a) Topograph, (b) Magnetic Phase (c) amplitude (d) TM deflection image

Topographic and magnetic images of Ni deposition are showing in the fig 4.9 at -1.3V and -1.5V. Fig.4.9 is the topographic and magnetic images taken over the same area. The topography of the sample shows a large number of the spherical grains. As Nickel is a ferromagnetic material, the magnetic domain structure in the Nickel thin films is shown in Figure. From the figure in phase mode, magnetic contrast was observed in the magnetic force images. It can be seen that the image is characterized by darker areas adjacent with brighter areas in submicron scale and in random distribution. These dark dots are iron grains of 200–400nm size. The magnetic tip magnetized these grains, producing attractive force between the tip and the Ni grains. Therefore, only the black regions can be observed. In some sense, the brightness of the local black regions reflects the depth of the ferromagnetic phase embedded in the film sample. The magnetic image in the TM deflection mode shows, the tip-cantilever is driven with close resonance frequency. TM Deflection containing top-bottom laser beam unbalance detected signal from the cantilever. Fig contains wavy artifacts. Its presence is connected to high reflectance of the surface and high, steep features causing unwanted interference, what disturbs a detection process. Thereby we can see a combination of real and not existing objects. From the figure at both -1.3V and -1.5V, we can observe, the magnetic images for the -1.3V is better than the image at -1.5V, although the grain size is finer.

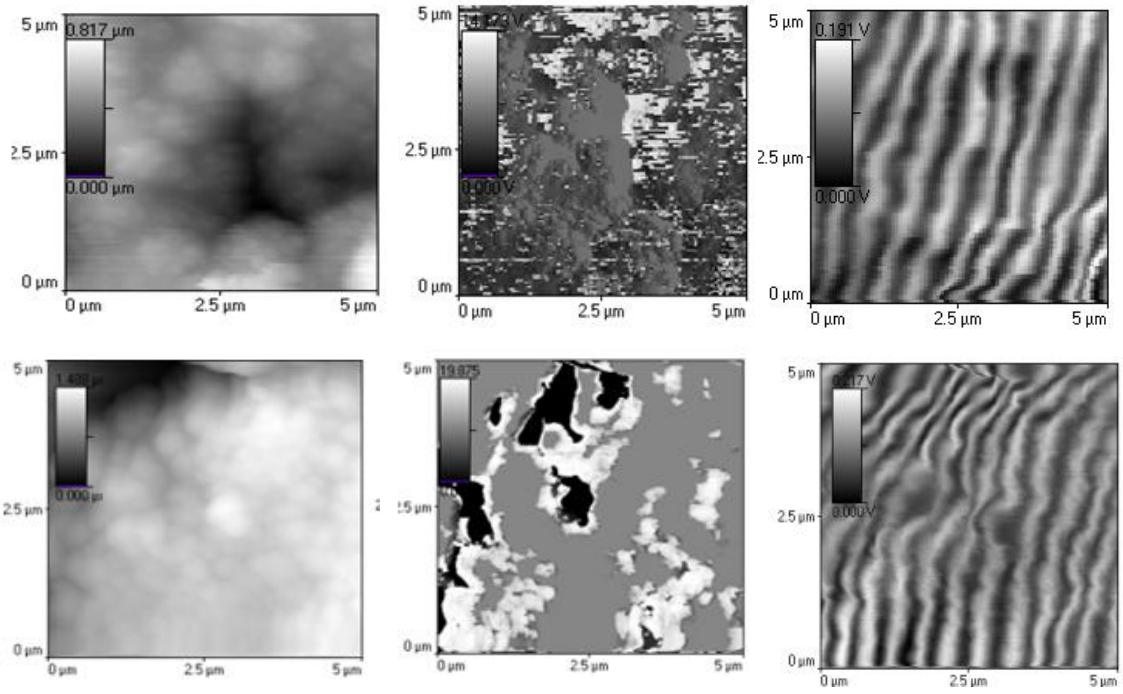

Fig (4.9): MFM of Ni at (a)-1.3V (b) -1.5V

Table 4.4: Roughness factor and grain size distribution from MFM topography Measurement of Cu, Co & Ni deposits:

Material	Potential (v)	Roughness factor (nm)	Grain size distribution (nm)	Avg.Height (nm)
Cu	-1.2	158	95-249	499
Co	-1.2	773	482-902	836
Ni	-1.3	180	107-203	534
	-1.5	185	43-193	683

4.2. Co-Cu Magnetic Alloy thin film:

4.2.1. Cyclic Voltammetry:

Fig 4.10(a), shows the coupled cyclic voltammograms for Co, Cu and Co-Cu alloy for the deposition and dissolution phases onto graphite substrate at the scanning range of -1.6V to +2V at a scan rate of 10mV/sec. Fig 4.10(b), represents the voltammogram of Co-Cu alloys in solution 1, 2, 3 as shown in Table-3.1. For cobalt deposition there is no negative current produced until the potential reaches to -0.56V vs. SCE, which is also the crossover potential for the system. At this voltage, the cathodic current starts to increase and forms the reduction peak at -1.315V vs SCE. Then the current increases to the vertex potential -1.6V vs SCE without any noticeable change. The reduction peak detected at -1.315V, may be the Co reduction. Then the subsequent increase in current values may be ascribed to hydrogen evolution, but the EDS analysis (not shown) shows no visible percentage of the said element in the deposit, hence that may attributed to further reduction of Co past the peak.

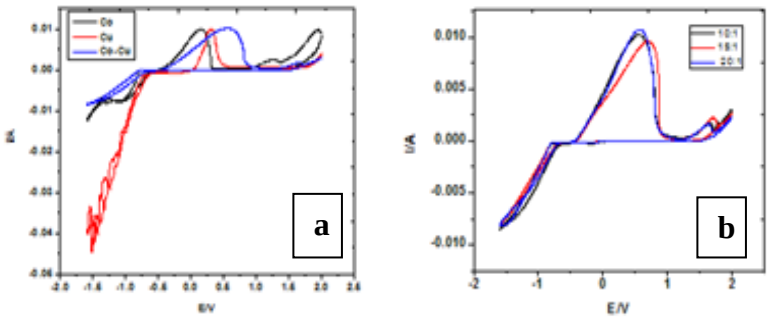

Fig (4.10): Cyclic voltammogram of Co-Cu alloy

The cathodic current gradually decreases until it crosses 0 V and turns into anodic current. Upon sweep reversal, metal already deposited on the electrode surface continues to grow as a result of the $Co^{2+}+2e^- \rightarrow Co(s)$, reaction remaining thermodynamically and kinetically favorable. Further sweep in the +ve direction, results in the abrupt anodic peak at +0.158V vs SCE which is the dissolution peak. The early dissolution and delayed deposition of metal confirms the active nature of the metal. The current past the peak at a potential of +0.52V vs SCE, may be due to oxygen evolution at electrode surface. The presence of crossover is diagnostic for the nuclei and growth phase on the electrode. Here $E_{pc,\,Co} - E_{pa,\,Co} > 70$ mV, indicating nuclei and growth phase formation in mixed mass and charge controlled (Quasi-reversible process) phenomena, further $I_{c,Co}/I_{a,Co} = 1.38$. For Copper, the reduction peak appears at -1.505 V for Cu at 0.02 M. The crossover potential forms at the potential of +0.17 V vs SCE. Here for the reduction couple, $E_{pc,\,Cu} - E_{pa,\,Cu} > 70$mV, indicating Quasi-reversible process. The CV scans with decreasing Cu Concentration (not shown) shows no noticeable changes in the reduction peak. But the oxidation peaks have shifted to more +ve potential as the Cu concentration increases in the solution. This may be due to the high availability of Cu ions in the ionic atmosphere. Now analyzing the reduction and oxidation kinetics of the alloy, the alloy has got reduced without any reduction peak and has consumed less charge than both of the metals for the same –ve potential limit. This may be an indication of steady and irreversible incorporation of the metals in the alloy lattice during metal discharge. The alloy oxidized near pure cobalt oxidation, which may be an indication for a copper rich alloy composition at low cathodic limit and more Co incorporation at higher cathodic potentials. Hence to explore the potential effects, depositions were carried out at potentials of −1.2V, −1.4V and −1.6V. Further there is a shift of the alloy anodic peak with Cu concentration variations in the bath.

To analyze the cathodic efficiency of cobalt deposition, the charge due to cathodic (Qc) and anodic (Qa) processes can be obtained from integration of the cathodic and anodic branches of the I-E curves. The Qa/Qc ratio for the Co deposition from the solution is found to be 0.79. This indicates that Co deposited during the cathodic sweep potential is not totally oxidized during anodic scan. Faradic efficiency increases with increasing copper concentration in the solution as obtained by the experiment. Cathodic efficiency of Cu is 0.16 for 0.04M Cu concentration. Similarly for the Co-Cu alloy, the cathodic efficiency is 1.07 for 0.04M Cu

concentration in the alloy solution. This over efficiency indicates that, other simultaneous reactions have occurred at the anode surface. That may be oxygen evolution at the anode surface.

4.2.2. Chronoamperomatry:

The current transients are recorded for the alloy at constant Co and different copper concentration for different deposition potentials of −1.2 V, −1.4 V, −1.6 V for 20 sec. From fig 4.11, it can be clearly seen that the shape of the current transient has strongly affected by Cu concentration and deposition potential variations. The general shape of the curves in Fig. 4.11 is due to the fact that initial nucleation results in a rapid increase in reduction current. Ion reduction occurs more rapidly than ion diffusion to the surface, resulting in a depletion of ion concentration near the surface. This then leads to a decrease in reduction current until a steady state is achieved at longer deposition times.

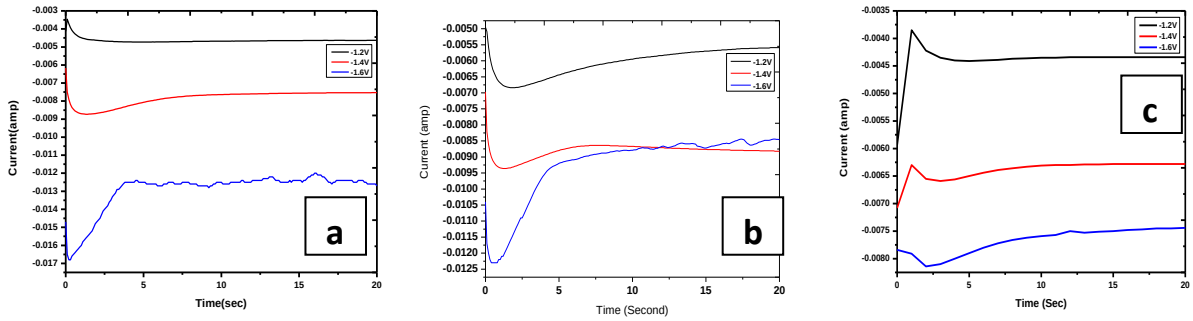

Fig (4.11): Chronoamperometry of Co-Cu at (a)0.04M Cu, (b) 0.03M Cu and (c) 0.02M Cu with 0.5M Co.

The value of current maxima has increased with potential for all the concentration ranges. Further the data in fig. 4.11 indicates that only at −1.6 V is the initial deposition rate faster than the rate of metal ion diffusion to the surface for all the compositions of the depositing bath. At lower deposition potentials for 0.02 M Cu concentration, there is a dominancy of non-faradic current due to double layer charging indicating lower amount of alloy deposition on the substrate for all the potentials. However, at lower potentials there is decrease in the ion reduction current is observed at pulse duration times up to 20 s, indicating that the reduction rate is slower than the rate of diffusion of ions to the electrode surface. Additionally, there is a significant increase in the maximum reduction current observed with increasing Cu ion concentration in the electrodepositing alloy bath. Hence, the results signify nucleation time was shorter for high

negative potential and high Cu concentration bath. This may be an indication of better deposit at higher deposition potential for high Cu concentrations as discussed in the next section of structural and morphological analysis. The established method of current transient analysis could explain the mode of deposition. The method relies on determining the gradient of a region of the log (current) Vs log (time) plot corresponding to the rising section of the transient plot. The slope of log (current) Vs log (time) varied from 0.2 to 0.8, which indicates instantaneous nucleation process for all the deposition kinds.

4.2.3. XRD Analysis:

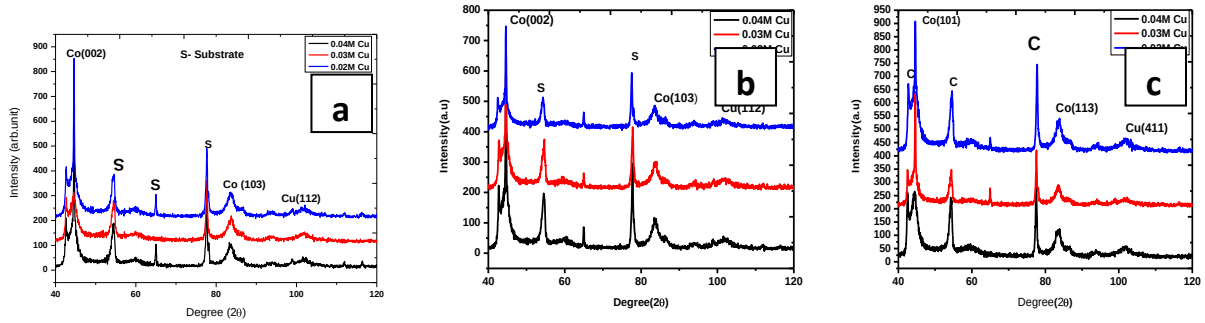

Fig (4.12): XRD of Co-Cu alloy at (a) -1.6V (b) -1.4V (c) -1.2V at different Cu concentration at 25°C

In the fig 4.12(a), Co peaks are at 44.16° and 83.13° attributed to (002) and (103) observed. Whereas Cu peak at 103° attributed to (112) is observed. The crystallite size and corresponding lattice strain for Co-Cu alloy on the graphite substrate at 25°C with different Cu concentration are shown in Table 4.5.

Table 4.5: Crystallite size and lattice strain of Co-Cu alloy films:

Potential (Volt)	0.04M Cu		0.03M Cu		0.02M Cu	
	Crystallitesize(nm)	Strain	Crystallitesize(nm)	Strain	Crystallitesize(nm)	Strain
-1.2	354	0.019	225	0.033	211	0.039
-1.4	155	0.009	186	0.041	206	0.042
-1.6	105	0.003	133	0.015	127	0.048

4.2.4. SEM (Morphological) Analysis:

Fig 4.13 shows the Co-Cu alloy morphology as a function of deposition potential and Cu concentration in the bath. It is clear that the Cu concentrations and deposition potentials modified

the electrodeposition process from the electrochemical analysis. In order to determine whether these changes were reflected in the deposit morphology and composition, an SEM/EDS study was performed. Table- 4.5 shows the variation of composition of Co and Cu in the deposits from the sulphate bath.

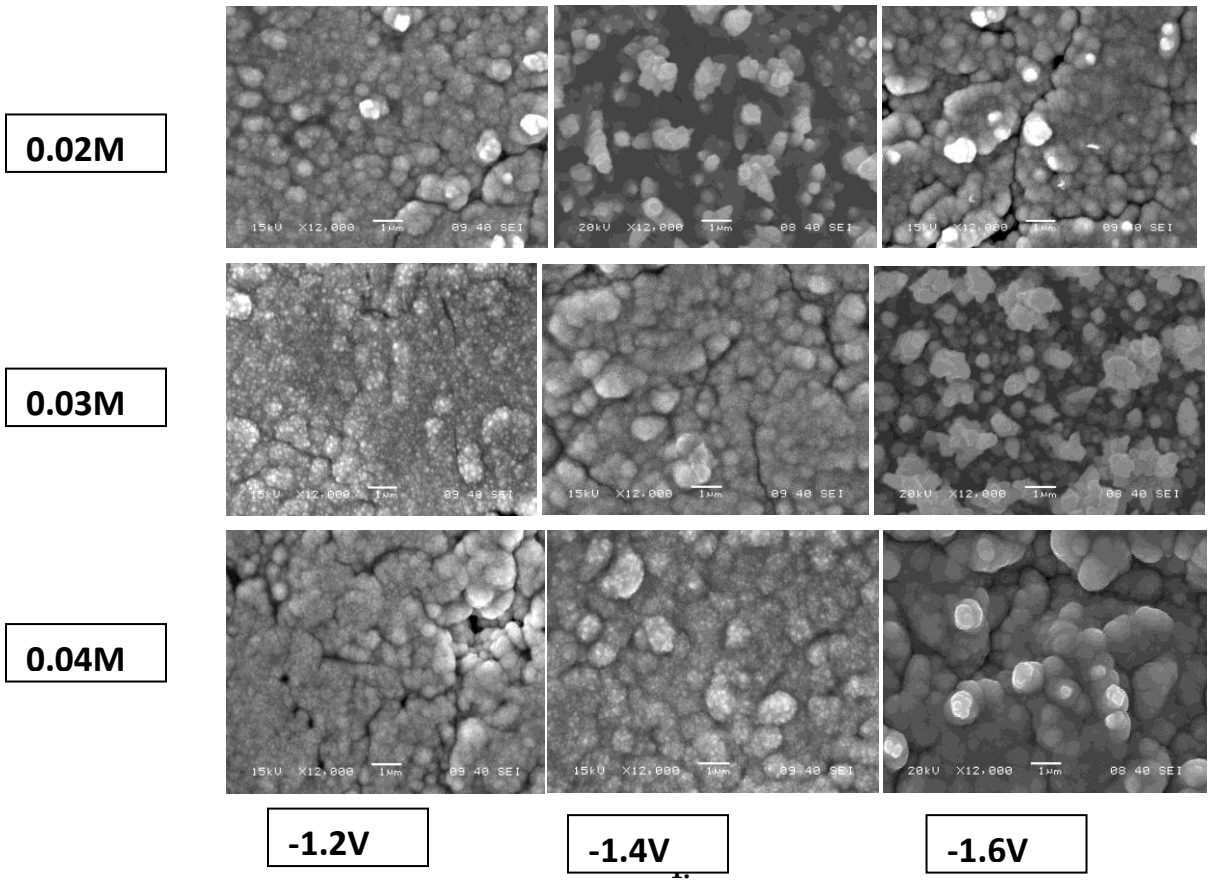

Fig(4.13): SEM of Co-Cu alloy at different Cu concentration and deposition potential

The SEM of the film grown at 0.02 M shows the formation of Cu/Co nuclei with a complex geometry, generally larger than 1 μm in diameter. As the copper concentration in the sulfate solution increases, bath results in formation of many small three-dimensional nuclei with an average diameter less than 1 μm. Deposits have relatively uniform surfaces with increased Cu concentration. These data indicate that deposition at 0.04 M Cu concentration leads to the formation of many small nodular nuclei and a relatively uniform coverage of the graphite substrate, while lower concentrations result in non-uniform dendritic deposits. Fig. shows the changes in the Co/Cu film surface morphology grown on the graphite when deposited at two different voltages viz. −1.2 V, -1.4V & −1.6 V for 20 s. The alloy films are reasonably uniform

with cleavage and agglomerated grain but exhibit rough morphology for all the ranges of applied voltages. The films have grown continuously even at low deposition potential. At -1.6V for all concentration, the particles are smaller in size and agglomerated.

Table-4.6: Co-Cu Alloy composition from EDS:

Potential (Volt)	**Cu Concentration**					
	0.04M		**0.03M**		**0.02M**	
	Co (wt %)	Cu (wt %)	Co (wt %)	Cu (wt %)	Co (wt %)	Cu (wt %)
-1.2	54	32	79	26	82	17
-1.4	66	26	65	35	53	37
-1.6`	86	14	70	11	67	8

Co content in the films varies in between 54 and 86.03 wt% with increased Cu concentration from 0.02 to 0.04 M. By varying the deposition potential from 1.2 to 1.4 V for the film deposited at 0.04 M Cu concentration, the alloy was found to get richer in Cu at low potential values. This certainly agrees with the electrochemical analysis. Hence it can be clearly seen from the images and EDS compositional analysis that the best magnetic morphology results when alloy was deposited at −1.6 V for the copper concentration of 0.04 M. The EDS analysis of Co-Cu alloy is given in the Fig (4.14).

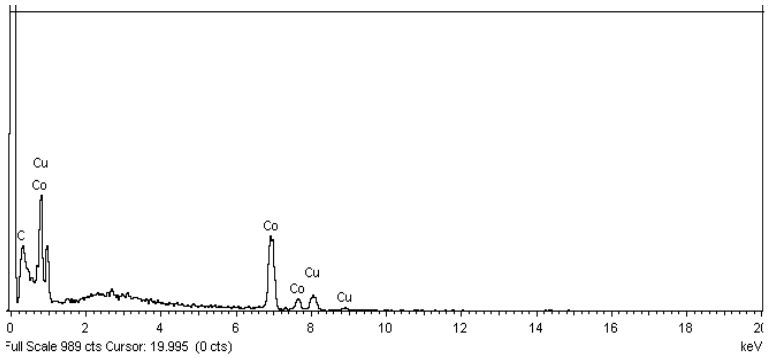

Fig (4.14): EDS spectra of Co-Cu alloy

The above observations can be explained in the following lines: the crystal structure variations and electrochemical reducibility level between the two depositing metals might have not allowed

an ease discharge and incorporation of the hexagonal Co in the FCC Cu system. However, when the deposition potential is made more negative, the Fermi-level of the substrate will be quite above the lowest occupied molecular orbital (LUMO) of the reducing Co ions. Hence, the deposition and charge reduction would have been progressed with less energy barriers at high potentials. And the clash of initial high availability of reduced species near the electrode's double layer might have caused a good amount of magnetic cobalt deposition in the non-magnetic metal matrix.

4.2.5. MFM (Magnetic) Characterization:

The surface texture and magnetic structure analysis was done under MFM dynamic conditions using the sequential two-scan method. In the first scan a topographic image is produced with a magnetic tip using tapping mode. In the second scan the cantilever is lifted to a selected height (usually in the range of 30-60 nm) and follows the stored topography without feedback (lift mode). During this second scan, as Van der Waals' forces vanish, tip–sample interactions are caused solely by magnetic effects. Under these conditions, the variations in phase, amplitude or resonant frequency are directly related to the local magnetic force derivative [49]. In lift mode the tip–sample separation (Z) was kept around 50 nm. The surface topography MFM images of the alloy films are shown in fig. 4.15 for Cu concentrations of 0.02, 0.03 and 0.04 M respectively. The topographic figure indicates the presence of aggregates of different sizes on the electrode surface. As the Cu concentration increases the size of the clusters decreases gradually. Further the surfaces appear to be smoother with the same trend. The average surface roughness (R_a) of the films varies in between 164 to 122 nm. The corresponding magnetic images are presented in the fig. In the present study, the magnetic force derivative was assessed through the phase variation and deflection in the resonant frequency of the scanning cantilever magnetic due to the higher spatial resolution of these signals than the amplitude shift signal [32]. The magnetic phase images can characterize the presence or absence of magnetic phases with the domain orientations, while deflection signal can signify the state of dipole moments. However, the MFM measurements presented here can only provide a qualitative measure of the domain magnetizations and stray fields.

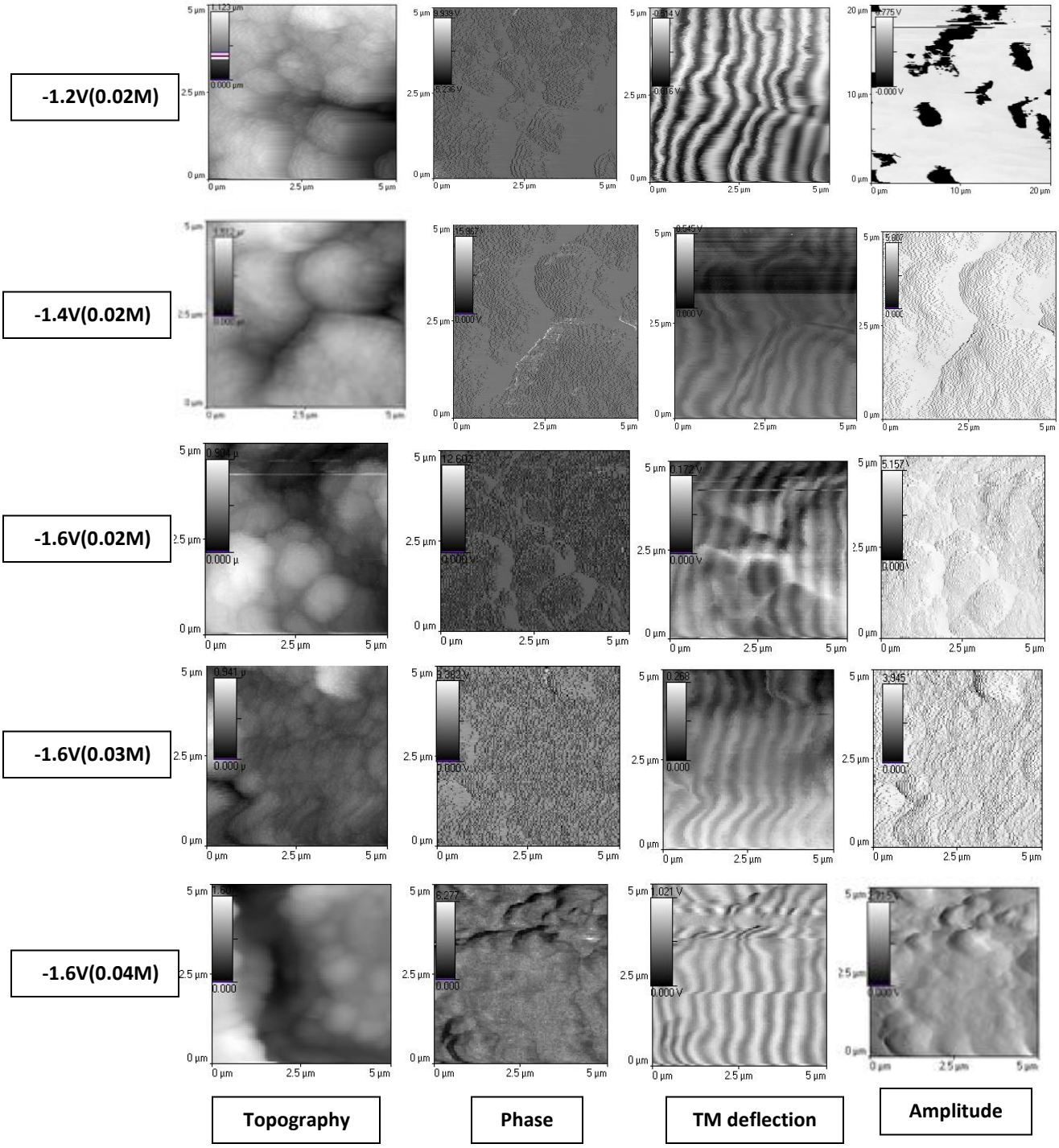

Fig (4.15): MFM Topographic and magnetic images of Co-Cu alloy at different condition

In fig. visible changes in the alloy surfaces can be observed as a function of Cu concentration. The films contain two distinct areas, one plane and the other with random fluctuations. The plane regions are assumed to have no contribution to the phase shift of the tip, remarked as non-magnetic phase i.e. the copper rich region in the alloy. Thus, the surface contains the magnetic

Co and non-magnetic Cu regions. Further, the heighted expanses have bright as well as dark portions. The color contrast within the aggregates suggests different magnetic domain regions. The bright color corresponds to repulsive interaction whereas a dark color corresponds to attractive interactions. With a downward tip magnetization, black corresponds to an upward pointing sample stray field, and white, to a downward field. Each alternation in the MFM signal marks the transition to another domain. As Cu concentration decreases in the alloy solution, the domains are larger in size. Moreover, at 0.04 M there is reduced attraction (only bright) and higher concentration deposits have mixed forces of interactions with multi domain vortex system. These could be due to the presence of other elements in the electrolyte and possibly have been co-deposited, which has not been possibly detected in the EDS spectra due to very low atomic contributions. Now considering the dipole moment system in the films, bright and dark stripe-like regions in the image can be observed for all the conditions. However, the stripe patterns are more prominent for the Cu molarity deposition indicating a permanent dipole moment magnetization in the alloy. The alternative stripe patterns are due to the out of plane magnetic domains separated by the 180° domain walls, dark part being visible due to low resolution. Large negative shifts in the resonance frequency are black and large positive shifts in the resonance frequency are white. The above complicated issues are further simplified by analyzing a small pure magnetic region with their corresponding line measure analysis for the same line (94^{th} line here) as given in fig. 4.16. A large shift in the line of topography (fig. 4.16 aii) to the phase (fig. 4.16 bii) can be observed from the figures. And a very systematic variation in the frequency shift (fig. 4.16 cii) can be elucidated. Hence, the domain magnetization seems to be oriented approximately normal to the grain surface. The magnetic domains are aligned almost parallel to each other.

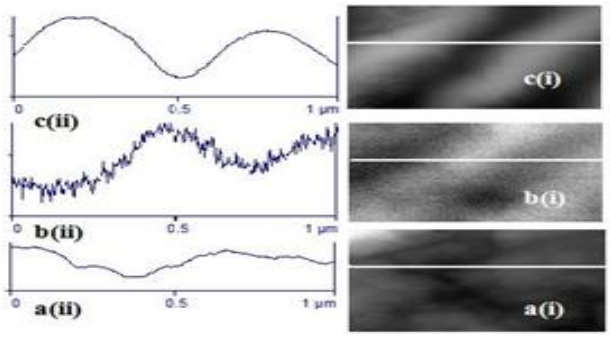

Fig (4.16): Line measure analysis at -1.6V for all concentration

Figure 4.15 also shows the effect of deposition potential on the film's magnetic structure distribution. Films with rich non-magnetic regions (Cu) were deposited at low negative reduction potentials. Again the ratio of bright to dark regions, of both phase and deflection variations, have become equalized for the upper limit (−1.6 V) of the deposition overpotential, indicating uniform magnetization.

Table 4.7: Roghness factor and grain size distribution of Co-Cu alloy from MFM topographic measurement:

Conc.(M)	Potential (V)	Grain size distribution (nm)	Roughness factor (nm)	Average height (nm)
0.02	-1.2	131-389	171	659
	-1.4	120-313	217	862
	-1.6	97-227	290	1206
0.03	-1.6	94-239	79	334
0.04	-1.6	156-221	122	591

4.3. Ni-Cu Magnetic Alloy thin film:

4.3.1. Cyclic Voltammetry:

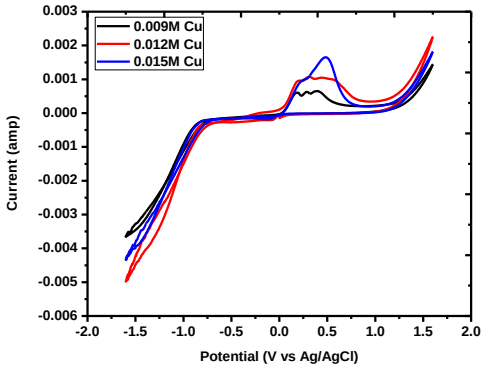

Fig (4.17): Cyclic Voltammogram of Ni-Cu allot at different Cu concerntration at 25°C at a scan rate 10mv/Sec

Fig (4.17) shoes the Cyclic voltammograms for Ni-Cu alloy for the deposition and dissolution phases onto graphite substrate at the scanning range of -1.6V to +1.6V at a scan rate of 10mV/sec in solution as shown in Table-3.1. The alloy has got reduced without any reduction peak and has consumed less charge. This may be an indication of steady and irreversible

incorporation of the metals in the alloy lattice during metal discharge. There are no remarkable differences in the reduction peaks at different Cu concentration. But there is shift of dissolution peak (anodic peak) towards more positive potential as Cu concentration in the alloy bath increases. It is reasonable to believe that the initial high availability of ions in the ionic atmosphere as the Cu concentration increases, so the alloy oxidized at higher overpotential. Again there is an increase in the anodic peak area as the Cu concentration is increases. We can observe from these facts that, overpotential of the anodic process is practically independent of concentration, however, the overpotential corresponding to the cathodic peak is not. For 0.015 Cu concentrations, only one dissolution peak is present, indicating only the metal dissolution reaction at the electrode surface. There are two crossovers are present at a potential -1.186V vs SCE and -0.739V vs SCE respectively. The anodic peaks are at potentials of 0.990V vs SCE, 0.196V SCE and 0.288V vs SCE for 0.009M, 0.012M and 0.015M respectively.

To analyze the cathodic efficiency of alloy deposition, the charge due to cathodic (Qc) and anodic (Qa) processes can be obtained from integration of the cathodic and anodic branches of the I-E curves. The Qa/Qc ratio for the alloy deposition from the solution at 0.009M Cu concentration is found to be 0.32. This indicates that alloy deposited during the cathodic sweep potential is not totally oxidized during anodic scan. Faradic efficiency increases with increasing copper concentration in the solution as obtained by the experiment

4.3.2. Chronoamperometry:

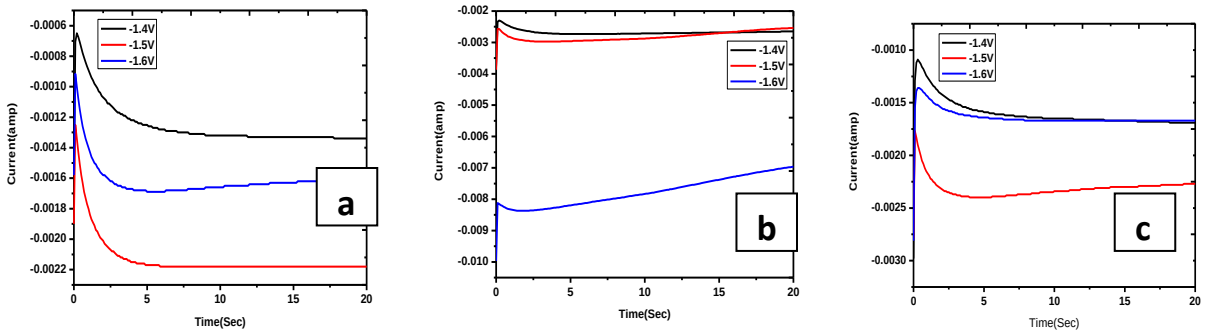

Fig(4.18): Chronoamperometry of Ni-Cu at(a)0.009M Cu,(b) 0.012M Cu and(c) 0.015M Cu with 0.175M Ni.

Current transients are recorded for Ni-Cu alloy at different Cu concentration at 0.175M Ni in Fig 4.18. In fig 4.18(a), there is a dominancy of non-faradic current due to double layer charging

indicating lower amount of alloy deposition on the substrate for all the potentials and for all Cu concentration. After the double layer charging, the current increases rapidly to a maximum where the alloys are reduced and form the alloy nuclei at the electrode surface. Then the subsequent fall of current occurs which indicate the growth of the nucleai at the electrode surface. In fig 4.18(a) and (b), for cu concentration, 0.009M and 0.012M respectively, as the negative overpotential increases the reduction current increases and nucleation time is shorter. But in fig 4.18(c), at -1.5V, the current is maximum and nucleation time is shorter. Again at 0.009M Cu concentration, maximum current is achieved. Hence, the results signify nucleation time was shorter for high negative potential and low Cu concentration bath.

4.3.3. XRD Analysis:

Fig (4.19) shows the XRD patterns of Ni-Cu alloy at different Cu concentration and deposition potential on the graphite electrode at 25°C. Fig shows the Ni and Cu peaks with the peaks from substrate material. The alloy film thickness is less than 1μm, so X-ray might have penetrated to the surface more pass the coating resulting the carbon identification. So the pure phase is not analyzed. The Ni peaks are at 44.23°, 78° and 84.24° attributed as (011), (103) and (112) are identified. Whereas Cu peak at 43.29° attributed to (111).

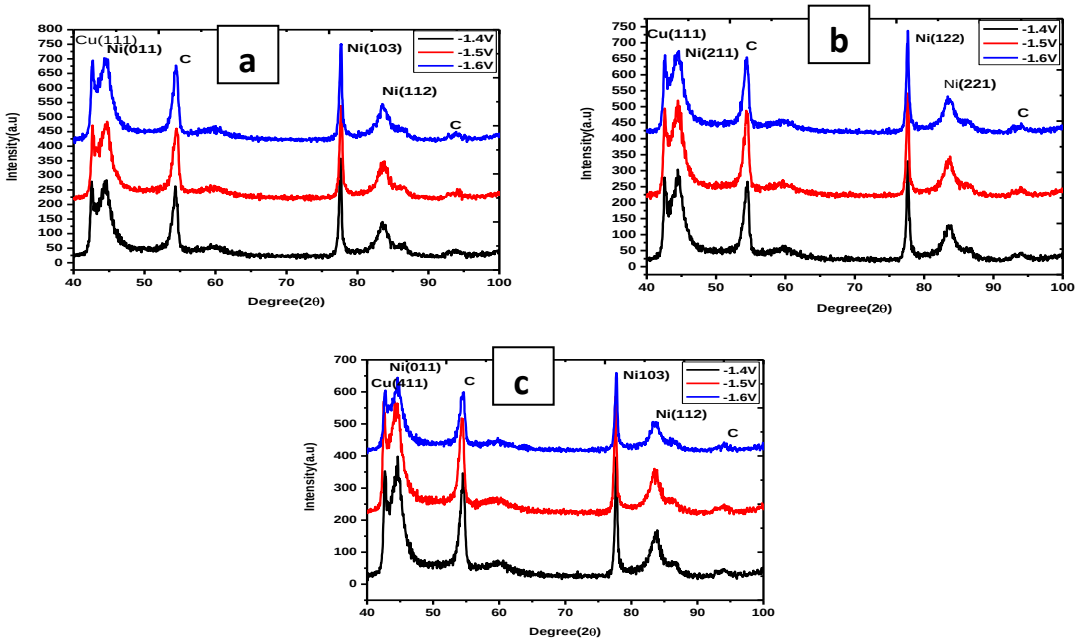

Fig(4.19): XRD of Ni-Cu alloy at (a) 0.009M Cu (b) 0.012M Cu (c) 0.015M Cu at different deposition potential at 25°C

The crystallite size and lattice strain is calculated by Williamson–Hall formula. The values are shown in the table 4.7.

Table 4.8: Crystallite size and lattice strain of Ni-Cu alloy films:

Potential (Volt)	0.009M Cu		0.012M Cu		0.015M Cu	
	Crystallitesize(nm)	Strain	Crystallitesize(nm)	Strain	Crystallitesize(nm)	Strain
-1.4	267	0.024	314	0.037	137	0.079
-1.5	216	0.008	298	0.047	146	0.002
-1.6	97	0.003	258	0.015	98	0.008

4.3.4. SEM (Morphological) Analysis:

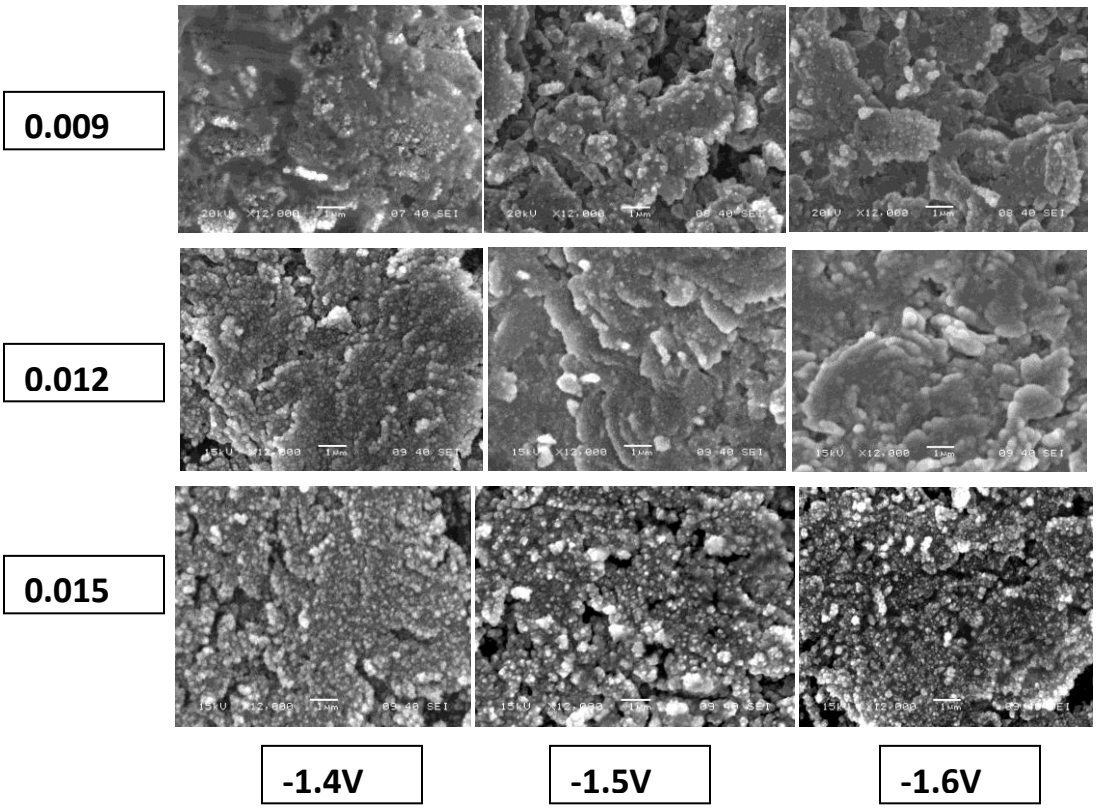

Fig(4.20): SEM of Ni-Cu alloy at different Cu concentration and deposition potential

Fig 4.20 shows the micrographs of Ni-Cu alloy obtained by electrodeposition from the sulphate bath at 25°C on the graphite substrate. Figure shows the regular structure is obtained. It is evident from the figure that the deposition is uniform throughout and exhibit a wavy like

appearence. The decrease in grain size with increase in deposition potential is clearly evidence. Figure revealed that deposit morphology was strongly dependent on the deposition potential and Cu concentration. As the Cu concentration increases in the electrolytic bath, the deposits are more uniform and dense. Nodular nuclei are formed at Cu 0.015M concentration. The morphology is changed from wavy layered structure to nodular structure. The EDS analysis in the table 4.8 shows the Ni and Cu composition in the bath at different potential and different Cu concentration.

Table-4.9: Ni-Cu Alloy composition from EDS:

Potential (Volt)	**Cu Concentration**					
	0.009M		**0.012M**		**0.015M**	
	Ni (wt %)	Cu (wt %)	Ni (wt %)	Cu (wt %)	Ni (wt %)	Cu (wt %)
-1.4	18	7	42	19	38	19
-1.5	37	4	55	16	59	18
-1.6`	62	37	61	20	38	16

From the Table-4.8, it is clear that, as the deposition potential increases the impurity level decreases, and Ni-Cu wt% is more. Again when Cu concentration in the bath increases, impurity level increases in most cases. EDS spectra of Ni-Cu alloy is given in fig 4.21.

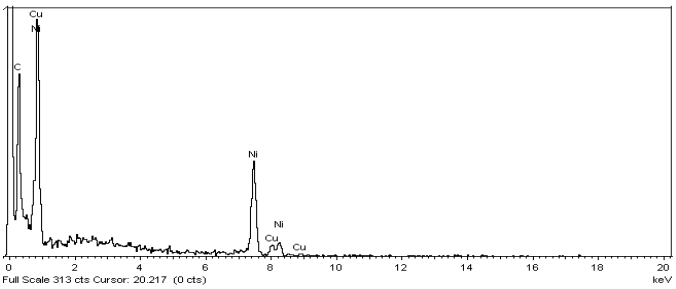

Fig(4.21): EDS spectra of Ni-Cu alloy

4.3.5. MFM (Magnetic) Characterization:

Analysis of several signals is the measurement performed in intermittent lift mode with Dilnnova instrument from Veeco for Ni-Cu alloy is shown in the fig 4.22. Topography, Phase (Phase Imaging) and TM Deflection (containing top-bottom laser beam unbalance detected signal from

the cantilever) and amplitude signals were acquired. The magnetic microstructure shows the presence of domains. Magnetic domains are of various kinds, and competitively contribute to the anisotropy energies. The transition region between the domains, called the domain wall, is not continuous across a single atomic plane.

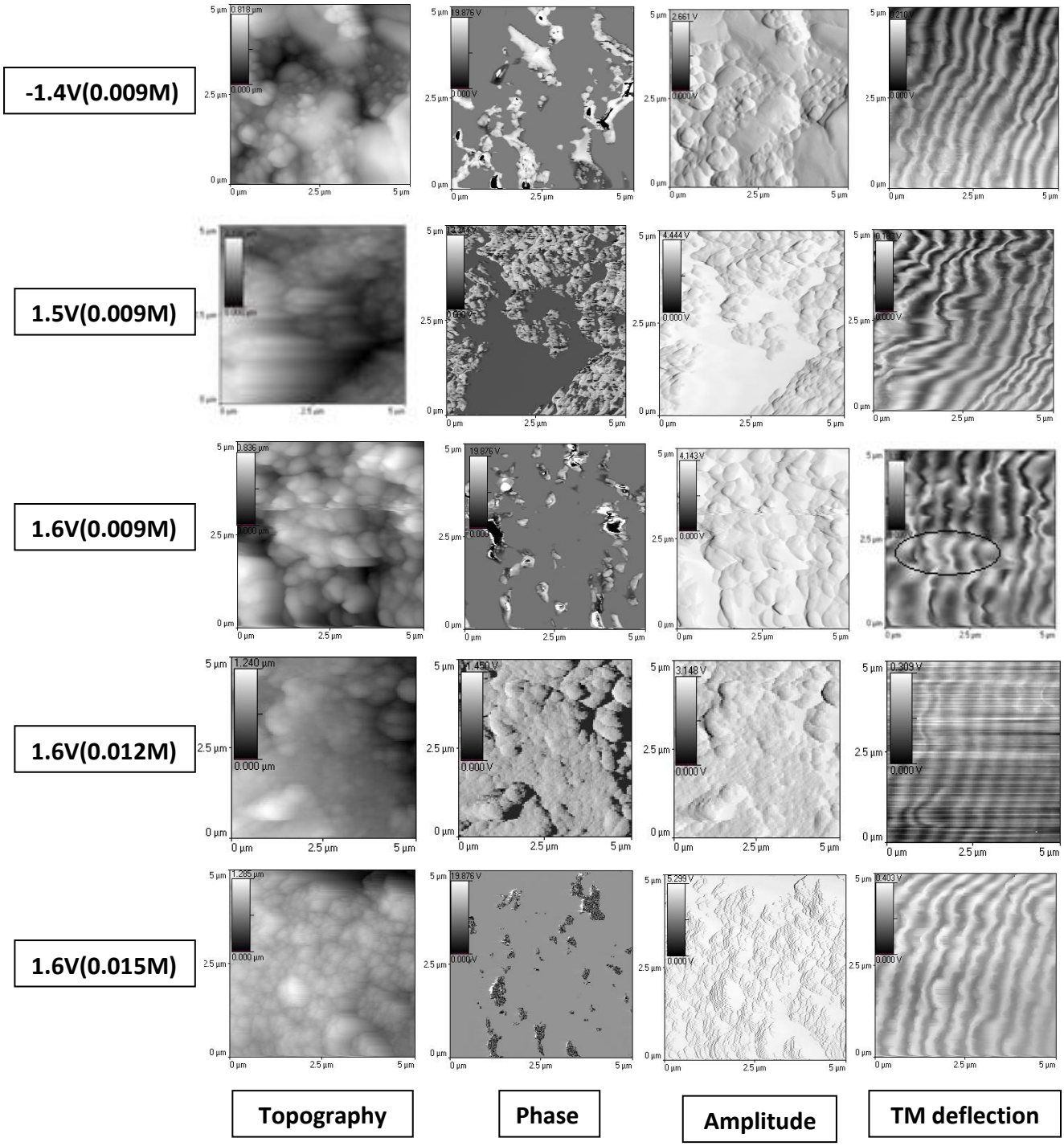

Fig (4.22): MFM Topographic and magnetic images of Ni-Cu alloy at different condition

Profiles of a domain wall can be defined according to the sign of the magneto static interaction between the local surface position and the tip. The images of Figs.4.22 indicate that the magnetic phase contains both single domain and multidomain states, which is strongly dependent on the deposition potential and Cu concentration in the alloy depositing bath. Fig. 4.22, TM deflection mode, illustrates the Bloch walls with the appearance of bright and dark lines. Ripples appear just when the tip scans across a strong domain wall, which appears tightly as the scan speed is faster and is direction dependent. Lowering down the feedback gain of the tip-scan can reduce these oscillations whilst with the loss of contrast. Similarly, the wavy wall that separate the front zone from the nonswitched area had also been observed in whisker-based tunnel junctions [89]. Figure shows the corresponding remanent magnetic microstructure of those double films. Because the MFM tip is perpendicularly magnetized, so the tip is sensitive to stray field gradients from *z*-orientated domains or the *z*-components of domains oblique to the sample surface. The weak stripe domain where bright to dark contrast arises from the magnetization canted up or down out of the films plane, confirms the presence of perpendicular anisotropy. The low contrast MFM images are characteristics of magnetic films which magnetization mainly lies in the film plane. The magnetic ripple structure, which is explained by local variations of the induced anisotropy due to a superposition of the uniaxial anisotropy of the film and the crystalline anisotropy of single crystallites, appears in these samples. The average roughness was found to be in the range 120nm to 331 nm. From the figure, it is clear that, phase mode and TM deflection mode of MFM gives the better magnetic image for the characterization. Clear visualization of magnetic structure is not possible with the amplitude mode. As the Cu concentration increases the size of the clusters increases gradually. Further the surfaces appear to be smoother with the same trend. The average surface roughness (R_a) of the films varies in between 120 to 219 nm. The bright color corresponds to repulsive interaction whereas a dark color corresponds to attractive interactions. With a downward tip magnetization, black corresponds to an upward pointing sample stray field, and white, to a downward field. At lower potential and lower Cu concentration in the alloy bath gives the better magnetic structure. But as Cu concentration decreases in the alloy solution, the domains are larger in size. Moreover, at 0.009 M there is reduced attraction (only bright) and higher concentration deposits have mixed forces of interactions with multi domain vortex system.

Table 4.10: Roghness factor and grain size distribution of Ni-Cu alloy from MFM topographic measurement

Conc.(M)	Potential (V)	Grain size distribution (nm)	Roughness factor (nm)	Average height (nm)
0.009	-1.4	129-419	129	445
	-1.5	115-395	219	776
	-1.6	96-315	120	429
0.012	-1.6	246-279	169	610
0.015	-1.6	261-379	139	768

These could be due to the presence of other elements in the electrolyte, which has not been possibly detected in the EDS spectra due to very low atomic contributions. At lower concentration and lower deposition potential, we observe much more intense and localized magnetic domains of nanometric size. At higher potentai and low concentration, interestingly, we did find regions in which the domain alignment was disrupted, and a typical closure domain was established, as illustrated by the circle in figure. A few magnetic defect lines were found on the MFM images due to the residual stresses resulting from the physical scratches; however, these scratches have little influence on the macro-domain structure analysis.

CHAPTER -5

Conclusions

Conclusions:

Copper, Cobalt and Nickel thin films along with Co-Cu &Ni-Cu magnetic alloy thin films were cathodically electrodeposited at various overpotentials on graphite (Asbury) electrode at different concentration. The deposits were characterized with X-ray diffractograms, microstructure analysis by SEM, composition of the alloy films by EDS, magnetic microstructure by Scanning probe microscope (MFM).

The observation and analysis of the results obtained from the above studies are enlisted as follows.

1. Cyclic Voltammograms (CV) was performed in different potential range to set the deposition potential and to identify the presence of electrodeposition process. For Co-Cu alloy deposition, the anodic peaks shifts to more positive potential as Cu concentration in the alloy bath increases due to high availability of Cu ions in the ionic atmosphere. And for Ni-Cu alloy, the peak current increases with the increase in Cu concentration in the alloy bath.

2. From current transient analysis, it was found that, number of active sites of nucleation for Ni is highest at -1.5V, and for Cobalt at -1.4V. For Co-Cu alloy, the value of current maxima has increased with potential for all concentration range. There is a significant increase in the maximum reduction current observed with increasing Cu concentration in the electrodepositiong alloy bath, signify nucleation time was shorter for high negative potential and high Cu concentration bath. For Ni-Cu alloy, nucleation time was shorter for high negative potential and low concentration.

3. The phases of the deposits are confirmed by the XRD analysis. It is indicated that the crystallite size decreases and lattice strain increases with the increase in the –ve overpotential for all the elemental (Cu,Co,& Ni) deposits. For Co-Cu alloy deposits, as the –ve potential increases, lattice strain increases and crystallite size decreases. Again for Ni-Cu alloy deposits Crystallite size decreases and lattice strain increases.

4. Surface morphology and microstructure shows the surface morphology is dependent on the deposition potential and concentration of the bath. EDS analysis for Co-Cu alloy shows, as negative overpotential and Cu concentration of the alloy bath increases, the impurity deposition is less. And for Ni-Cu alloy, as the potential increases and at low Cu concentration, impurity level decreases.

5. The magnetic phase images can characterize the presence or absence of magnetic phases with the domain orientations, while deflection signal can signify the state of dipole moments. In all phase shift images, plane as well as corrugated regions were observed. The plane regions were interpreted as non-magnetic as they didn't contribute to the shifting of the probe due to magnetic forces while corrugated regions were magnetic patches. Further these magnetic aggregates consist of dark and bright regional areas. The colour contrast within the aggregates suggests different magnetic domain regions. The bright color corresponds to repulsive interaction where as dark color corresponds to attractive interactions. With a downward tip magnetization, black color corresponds to an upward pointing sample stray field, and white, to downward fields. Deflection magnetic images give the state of magnetization. Very rough magnetic properties can be estimated from amplitude images.

6. Magnetic microstructure (MFM) analysis for Co shows, the roughness factor and grain size distribution is very high. For Ni deposits, at high overpotential, the grain size is low and roughness factor is higher. In Co-Cu alloy deposition, at high cu concentration and high negative overpotential, the magnetic microstructure is better, And Ni-Cu alloy deposits, at lower Cu concentration and low negative overpotential, the magnetic domain structure is better.

References

1. Sharma P, Gupta A, Ion beam Sputtered thin films of finement alloy for soft magnetic applications, Nuclear Instruments and Methods in Physics Research B 244 (2006) PP.105-109.
2. Agostinelli E, Laureti S, .Scavia G, Testa A.M., Study of Structural microstructural and magnetic property of very thin $Co_{50}Pt_{50}$ films deposited by PLD, Material Science And Engineering C 27 (2007) PP.1466-1469.
3. Nam H.S., Yakoshima Y., Nakanishi T, Osaka T., Yamasaki Y., Lee D.N., microstructure of electroplated soft magnetic CoNiFe thin films, Thin Solid Films 384 (2001) PP.288-293.
4. Panda A., Electrodeposition of Nickel–Copper alloys and Nickel-Copper-Alumina nanocomposites into deep recesses for MEMS, PhD Thesis, B.S. Anna University, The Department of Chemical Engineering, May, 2003.
5. Artorix de la Cruz de Ona, Determining the permeability of magnetic thin film material by Magnetic Force Microscopy: relation with Superconducting thin films, Physica B 348 (2004) PP.117-182.
6. Freeman A.J., Wu R.Q., Magnetism in manmade materials, Journal of Magnetism and magnetic materials, 104-107 (1992) PP.1-6.
7. Maeda Y.,Takei K,.Rojens D.J, Compositional Microstructure in Co-Cr films for magnetic recording, Journal of magnetism and magnetic materials, 137(1994)223.
8. Kobe S., Fechmin A.R., Nose H., Stobiecki F., Amorphous magnetism and metallic magnetic materials-Digest, Journal of magnetism and magnetic materials, 60(1986) PP.1-135.
9. Stadelmaier H.H., Magnetic properties of materials, Material Science and Engineering A 287(2000) PP.138-147.
10. Levy J.C.S., Structural features of magnetism in Amorphous materials, Journal of magnetism and magnetic materials, 54-47(1986) PP.277-278.
11. .Varga L.K, Mazaleyrat F., Kovac J., Kakey A., Soft magnetic properties of nanocrystalline $Fe_{100-x}Si_x$ ($15<x<34$) alloy, Journal of magnetism and magnetic materials, Vol 215-216 (2000) PP.1210123.

12. Liu M., Han G.B., Yang W., Gao R.W., Dependence of Coercivity on the intergranular phase for nanocrystalline Nd-Fe-B magnet, Journal of Alloys and compounds 486 (2009) PP.257-260.
13. Aich S., Shield J.E., Effect of Nb and C additives on the microstructures and magnetic properties of rapidly solidifies Sm-Co alloys, Journal of Alloys and Compounds, 425 (2006) PP.416-423.
14. Aich S., Shield J.E., Effect of Wheel speed on the microstructure and magnetic properties of rapidly solidified Sm-Co alloys, Journal of Alloys and Compounds, In press, Accepted manuscript, available online May 2010.
15. Koon N.C., Williams C.M., Das B.N., Giant Magnetorestriction materials, Journal of magnetism and magnetic materials, 100(1991) PP.173-185.
16. Min S.R., Chao H.N., Kim K.W, Chao Y.J., Cha S.H., Chung C.W., Etch Characteristics of magnetic Tunnel junction stack with nanometer sized patterns for Magnetic Random Access Memory, Thin Solid Films, 516(2008) PP.3507-3511.
17. Kim J.H., Grishin A.M., Wet and Dry etching of $La_{0.67}(Sr, Ca)_{0.33}$ MnO_3 films on Si, Thin Solid Films 515 (2006) PP.587-590.
18. Gonzalez O.J., Bistue G., Castano E., Gracia F.J., Room temperature Collossal Magnetoresistance of nanocrystalline $La_{0.67}Sr_{0.33}MnO_3$ Sputtered thin films, Journal of magnetism and magnetic materials, 222, (2000), PP 199-206.
19. Zhung Y.H., Li J.Q., Huang W.D., Sun W.A., Ao W.Q., Giant Magnetocaloric effect enhanced by Pb-doping in $Gd_5Si_2Ge_2$ compound, Journal of Alloys and compounds 421 (2006) PP.49-53.
20. Vekilov Y.K., Isaev E.I., Johansson B., Diamagnetism in Quasicrystals, Solid State Communications 133, (2005), PP. 473-475.
21. Kotosonov A.S., Diamagnetism of Pyrolytic Carbon, Carbon, 25, (1987), PP. 613- 615.
22. Gryzinski M., Diamagnetism of matter and structure of the atom, Journal of magnetism and magnetic materials, 71, (1987), PP.53-62.
23. Goldstein L., On the theory of Paramagnetism, Annals of Physics, 15, (1961) PP.141-156.
24. Won H., Jang H., Maki K., Pouli Paramagnetism in d-wave semiconductors, Physica B: Condensed Matters, 281- 282,(2000), PP.944-946.

25. Sundaresan A.,.Rao C.N.R, Ferromagnetism as a universal feature of Inorganic nanoparticles, Nano Today 4 (2009) pp.96- 106.
26. Fabrizio M., Giorgi C., Morso A., A Thermodynamic approach to Ferromagnetism and Phase Transitions, International Journal of Engineering Science, 47, (2009), pp.821-839.
27. Hsich, C.T. Liu J.Q., Lue J.T., Magnetic Force Microscopy studies of domain walls in Nickel and Cobalt films, Applied Surface Science 252, (2005), pp.1899-1909.
28. Yue L., Li Z., Kirby R., Sellmye D.r, MFM studies of Interlayer exchange coupling in Co/Ru/Co films: Effects of Ru layer thickness, Ultramicroscopy 109, (2009), pp.1040-1043.
29. Taylor R.A., Jakubovics J.P., Astie B,, Degauque J,, Direct Observation of the Interaction between Magnetic domain walls and dislocation in Iron, Journal of Magnetism and Magnetic Materials 31-34, (1983), pp.970-972.
30. Brandl A.L., Denardin J.C., Knobel M., Dotto M.E.R., Kleinke M.U., Study of Interactions in Co-SiO_2 granular films by means of MFM and magnetization measurements, Physica B 320, (2002), pp.213-216.
31. Carey R., Isaac E.D., Magnetic domains and techniques for their observation, The English University Press Ltd, London (1966).
32. Cullity, Graham C.D., Introduction to magnetic materials, 2nd edition, New York, Wiley-IEEE, pp.116.
33. Zablotskii V.A., Lamonova K.V., Mamalui Y.A., Frustration in the system of bent domains of a thin magnetic films, Physica B 205,(1995), pp.371- 378.
34. Piotrowski K., Szymczak R., Maziewski A., Temperature dependence of bubble domain structure in $YCrO_3$, Journal of magnetism and magnetic materials, 15-18, (1980), pp.1541- 1542.
35. Gavriliuk A.A., Mokhovikov A.Y., Semirov A.V., Semenov A.L., Turik N.V., Kudrewcev V.O., Stability of magnetic domains inside the core of amorphous wire, Journal of Non-Crystalline solids 354, (2008), pp.5230-5232.
36. Zotova S.G., Karl H., Savan A., Feydt J., Wehner B., Walther T., Zotov N., Stritzker B., Ludwig A., Structural and Magnetic Characteristics of FeCo thin films modified by combinatorial ion implantation" Thin Solid Films 495, (2006), pp.169-174.

37. Araujo C., Almeida B.G., Aguiar M., .Mendes J, A, Sructural and magnetic properties of $CoFe_2O_4$ thin films deposited by Laser Ablation on Si (001) substrate, Vaccum 82, (2008), pp.1437-1440.
38. Pattanaik G., Kirkwood D.M., Xu X., Zangari G., Electrodeposition of hard magnetic films and microstructures, Electrochimica Acta 52,(2007), pp.2755-2764.
39. http://en.Wikipedia.org/wiki/vibrating-sample-Magnetometer/09.05.2010.
40. Gramm K., Lundgren L., Beckman O., SQUID magnetometer for magnetization measurements, Physica Scripta, 13, (1976), pp.93.
36. http://www.npl.co.uk/quantum-phenomena/nanophysics/research/squid magnetometer/ 13.05.2010.
37. http://en.wikipedia.org/wiki/Magnetoresistance/13.052010.
38. Pane S., Gomez E., Valles E., Magnetostrictive Granular Cu-Co-Ni coatings prepaired by Electrodeposition, Journal of Electroanalytical Chemistry 596, (2006), pp.87-94.
39. Zhang D., Chung R., Karki A.B., Li F., Young D.P., Guo Z., Magnetic and Magnetoresistance behavior of solvent extracted particulate Iron/polycrylonitrile nanocomposite, Jornal of Physical Chemistry C, 114, (2010), pp.212-219.
40. Warda A., Wojtczak L., Wiatrowski G., Baldomer D., Pereiro M., Arias J.E., Magnetoresistance for thin multilayers, Physica Status Solidi (a), 32, (2003), pp.117-120.
41. Bostanjoglo O., Vieweger W., Low temperature Lorentz Microscopy on wear Ferromagnetics, Physica Status Solidi, 32, (1969), pp.311-321.
42. Balcerzak T., Jakuboviks J.P., Studies of Fe-Ni and Fe-Ni-Gd thin films by Lorentz microscopy, Physica Status Solidi, 101, (1987), pp.217-225.
43. Lozanne A.D., Application of Magnetic force Microscopy in nanomaterials Characterization, Microscopy Research and Technique, 69, (2006), pp.550-562.
44. Grutter P., Allenspach R.,Can Magnetic force microscopy determine micromagnetic structure?, Geophysical Journal International, 116, (1994), pp.502-505.
45. Schreiber S., Savla M., Pelekhov D.V., Icru D.F., Salku C., Chris P., Agarwal G., Magnetic force microscopy of Superparamagnetic nanoparticles, Small, 4, (2008), pp.270-278.

46. Salazar J.S., Romon H.A.C., Gomez L.B., Structural and magnetic domains characterization of magnetite nanoparticles, Materials Science and Engineering C 27, (2007), pp.1317-1320.
47. Proksch R., Recent Advantages in Magnetic Force Microscopy, Current Opinion in Solid State and Material Science 4, (1999), pp. 231-236.
48. Moina C.A., de Oliveira-Versic L., Vazdar M., Magnetic domain states in nano-sized Co nuclei electrodeposited onto monocrystalline silicon, Materials Letters 58, (2004), pp. 3518– 3522.
49. www.nuance.northwestern.edu/nifti/download/**MFM_manual**.pdf
50. Wijesundera R.P., Hidaka M., Koga K., Sakai M., Siripala W., Growth and Characterization of Potentiostatistically electrodeposited Cu2O and Cu thin films, Thin Solid Films 500, (2006), pp. 241-246.
51. Grijicic D., Pesic B., Electrodeposition of Copper: The nucleation mechanism, Electrochimica Acta 47, (2002), pp.2901-2912.
52. Waser R.M., Microstructure of Ceramic thin film, Current Opinion in Solid state and Material Science 1, (1996), pp.706-714.
53. Ma Y, Li X., Xie T., Wei F,, Yang Z., A study of Sputtering process for nanocrystalline FeAlN soft magnetic thin film, Material Science and Engineering B 103,(2003), pp.233-240.
54. Osaka T., Electrodeposition of highly functional thin films for magnetic recording devices of the next century, Electrochimica Acta 45, (2000), pp.2311-2321.
55. Signorini L., Riva M., Cantoni M., Bertacco R., Ciccacci F., Epitaxial $La_{2/3}Sr_{1/3}MnO_3$ thin films with unconventional magnetic and electric properties near the Curie temperature, Thin Solid Films 515, (2006), pp.496-499.
56. Wei G., Ge H., Huang L., Wu Q,, Wang X., Huang L., Influence of complexing agent on the electrodeposited Co-Pt-W magnetic thin films, Applied Surface Science 254, (2008), pp. 3425-3430.
57. Shinoura O., Koyanagi T., Magnetic thin film head with controlled domain structure by electroplating Technology, Electrochimica Acta, 42, (1997), pp.3361-3366.

58. Nam H.S., Yakoshima T., Nakanishi T., Osaka T., Yamazaki Y., Lee D.N., Microstructure of Electroplated soft magnetic CoNiFe thin films, Thin Solid Films 384, (2001), pp.288-293.

59. Feng L.J.,.Zhao Z, Ying Y.J., Hua Y.G., Chao C., Qing Z.J., Electrodeposition behavior of nanocrystalline CoNiFe soft magnetic thin film, Transactions of nonferrous Metals Society of China 16, (2006), pp.659-665.
60. Wesselinowa J.M., Magnetic field dependence of the dynamical properties of ferromagnetic semiconducting thin films, Solid State Communications 137, (2006), pp.278-281.
61. Qin G.W., Yang B., Xiao N., Ren Y.P., Jiang M., Zhao X., Oikawa K., Origin on Amorphization of Co-Mo magnetic thin films: Experiments and Thermodynamic Calculation, Thin Solid Films 517, (2009), pp.2984-2987.
62. Belhi R., Mliki N., Jomni S., Ayadi M., Abdelmoula K., Gergaud P., Clugnet G., Charai A., The Correlation between mechanical stress and magnetic properties of Cobalt ultra thin films, Thin Solid Films 414, (2002), pp. 119-127.
63. Mubarak A., Hamzah E., Toff M.R.M., Review of Physical Vapour Deposition (PVD) technique for hard coating, Journal Mekanical 20, (2005), pp. 42-51.
64. Moore J.H., Davis C.C., Coplan M.A., Building Scientific apparatus :A practical guide to design and Construction, Perseus Books, 1991.
65. Valade L., de Caro D., Sany J.P., Malfant I., Faulmann C., Almeida M., Fraxedas J., Brooks J.S., Thinfilm of molecular material grown on Silicon substrates by Chemical Vapour Deposition and Electrodeposition, Journal of Low temperature Physics 142, (2006), pp.397-400.
66. Lu Li, Lai M.0., Formation of the new materials in the solid state by mechanical alloying, Materials & Design Volume 16, (1995), pp. 33-39.
67. Baskaran I., Sankara Narayan T.S.N., Stephen A., Pulsed Electrodeposition of nanocrystalline Cu-Ni alloy films and evaluation of their characteristic properties, Materials Letters 60, (2006), pp.1990-1995.

68. Uhlemann M., Gebert A., Herrich M., Krause A., Cziraki A., Schultz L., Electrochemical deposition and modification of Cu/Co-Cu multilayer, Electrochimica Acta 48, (2003), pp. 3005-3011.
69. Azzaroni O., Schilardi P.L., Salvarezza R.C., Metal electrodeposition on Self-assembled monolayers: a versatile tool for pattern transfer on metal thinfilms, Electrochimica Acta 48, (2003), pp.3107-3114.

70. Allongue P., Maroun F., Metal Electrodeposition on single crystal metal surfaces mechanism, Structure and application, Current Opinion in Solid State and Material Science 10, (2006), pp.173-181.
71. Santos D. H., Garcia M.B.G., Garcia A.C., Effect of metals on Silver electrodeposition: Application to the detection of Cisplatin, Electrochimica Acta 50, (2005), pp.1895-1902.
72. Serebrennikova I., Vanysek P., Birss, V.I. Characterization of porous aluminum oxide films by metal Electrodeposition, Electrochimica Acta 42, (1997), pp. 145-151.
73. Motoyama M., Fukunaka Y., Sakka T., Ogata Y.H., Initial stages of Electrodeposition of metal nanowires in nanoporous templates, Electrochimica Acta 53, (2007), pp.205-212.
74. Zarpellon J., Jurea H.I., Klein J.J., Schreiner W.H., Mattoso N., Mosca D.H., Electrodeposition of Fe thin films on Si (111) surfaces in the presence Sodium saccharin, Electrochimica Acta 53, (2007), pp. 2002-2008.
75. Hyde M.E., Compton R. G., Theoretical and experimental aspects of electrodepositionm under hydrodynamic conditions, Journal of Electroanalytical Chemistry 581, (2005, pp.224–230.

76. Khelladi M.R, Mentar L, Azizi A, Sahari A, Kahoul A., Electrochemical Nucleation and growth of copper deposition onto FTO and n-Si(100) electrodes,Materials Chemistry and Physics, 115, (2009), pp 385-390.
77. Serebrennikova I., Vanjrsekt P., Birss V. I., Characterization of porous aluminum oxide films by metal electrodeposition, Elctrochimica Acta, 42, (1997), pp. 145-151,.
78. Scharifker B., Theotitical and Experimental Studies of multiple nucleation, Electrochimica Acta 28, (1983), pp. 879-889.

79. Orinakova R., Streckova M., Trnkova L., Rozik R., Galova M., Comparasion of Chloride and sulphate electrolyte in Nickel electrodeposition on the paraffin impregnated graphite electrode, Jornal of Electroanalytical Chemistry 594, (2006), pp.152-159.
80. Petersson I., Ahlberg E., Kinetics of the electrodeposition of Pb-Sn alloys Part II. At polycrystalline gold electrodes, Journal of Electroanalytical Chemistry 485, (2000), pp. 178–187.
81. Grujicic D., Pesic B., Reaction and nucleation mechanisms of copper electrodeposition from ammoniacal solutions on vitreous carbon Reaction and nucleation mechanisms of copper electrodeposition from ammonical solutions on vitreous carbon, Electrochimica Acta 50, (2005), pp. 4426–4443.
82. http://www.earlham.edu/~chem/chem341/c341_labs_web/cyclic_voltammetry.pdf/09.05.2010
83. http://en.wikipedia.org/wiki/Chronoamperometry/12.05.2010
84. Grujicic D., Pesic B., Electrochemical and AFM study of nickel nucleation mechanisms on vitreous carbon from ammonium sulfate solutions, Electrochimica Acta 51, (2006), pp. 2678–2690.
85. http://en.wikipedia.org/wiki/X-ray_crystallography/10.03.2010
86. http://en.wikipedia.org/wiki/Scanning_electron_microscope/24.12.2009.
87. http://en.wikipedia.org/wiki/Energy-dispersive_X-ray_spectroscopy/21.12.2009
88. http://en.wikipedia.org/wiki/Magnetic_force_microscope/12.04.2010
89. Hsieh C.T., Liu J.Q., Lue J.T., Magnetic force microscopy studies of domain walls in nickel and cobalt films, Applied Surface Science 252, (2005), pp. 1899–1909.